frontiers | Frontiers in Nuclear Engineering

TYPE Original Research
PUBLISHED 16 September 2025
DOI 10.3389/fnuen.2025.1655503

OPEN ACCESS

EDITED BY
Lakshmi Narayan Ramasubramanian,
Indian Institute of Technology Delhi, India

REVIEWED BY
Pavan A. H. V,
Bharat Heavy Electricals Ltd Research and Development, India
Surya Yadav,
Indian Institute of Technology (BHU), India

*CORRESPONDENCE
Asif Mahmud,
asif.mahmud@pnnl.gov
Isabella Van Rooyen,
isabella.vanrooyen@pnnl.gov

RECEIVED 28 June 2025
ACCEPTED 29 August 2025
PUBLISHED 16 September 2025

CITATION
Mahmud A, Meher S, Renner P, Rieffer A, Silva C, Snitzer J, Zhang Q, Lou X and Van Rooyen I (2025) Optimizing laser powder directed energy deposition for Grade-91 and Grade-92 ferritic/martensitic steels for nuclear applications: linking process parameters to microstructure. *Front. Nucl. Eng.* 4:1655503. doi: 10.3389/fnuen.2025.1655503

Optimizing laser powder directed energy deposition for Grade-91 and Grade-92 ferritic/martensitic steels for nuclear applications: linking process parameters to microstructure

Asif Mahmud[1]*, Subhashish Meher[1], Peter Renner[1], Ariel Rieffer[2], Chinthaka Silva[1], John Snitzer[3], Qianwen Zhang[3], Xiaoyuan Lou[3] and Isabella Van Rooyen[1]*

[1]Pacific Northwest National Laboratory, Richland, WA, United States, [2]University of Arizona, Tucson, AZ, United States, [3]Purdue University, West Lafayette, IN, United States

The nuclear industry is increasingly acknowledging the advantages of additive manufacturing (AM) due to its improved design flexibility and reduced manufacturing steps for producing complex engineering components. This study demonstrates the successful fabrication of nearly fully dense, nuclear-grade Grade-91 and, for the first time, Grade-92 Ferritic/Martensitic (F/M) steels via laser powder directed energy deposition (DED). Through rigorous process optimization, specifically tailoring laser power and scan speed, relative densities exceeding 99.8% were achieved in deposited 10 × 10 × 12 mm^3 blocks, yielding exceptional build quality. The resulting microstructures exhibited a characteristic lath martensite morphology, indicative of the rapid solidification inherent to the DED process. While both alloys showed this general microstructure, the addition of tungsten (W), slightly higher carbon content, and higher geometrically necessary dislocation (GND) density in Grade-92 significantly influences mechanical properties, evidenced by a substantial increase in Vickers hardness (425 ± 12 HV) compared to Grade-91 (386 ± 14 HV). Estimated yield strengths, derived from hardness measurements, were 1063 MPa and 1195 MPa for Grade-91 and Grade-92, respectively. These findings suggest DED as a viable and promising route for manufacturing high-performance F/M steel components tailored for demanding nuclear applications, paving the way for improved reactor designs and enhanced operational efficiency.

KEYWORDS

additive manufacturing, DED, F/M steels, process parameter optimization, vickers hardness

1 Introduction

The growing need for resilient materials capable of withstanding extreme mechanical and thermal stresses, coupled with intense neutron irradiation, is driving significant innovation in advanced manufacturing technologies, particularly Additive Manufacturing (AM) (Armas et al., 1998; Klueh et al., 2007; Shrestha et al., 2015; Zhou

et al., 2015; Henry and Maloy, 2017; Li et al., 2023; Cabet et al., 2019; Sridharan and Field, 2019a; Sridharan et al., 2019a; Kimura et al., 2020; Eftink et al., 2021a; El-Atwani et al., 2021; Villaret et al., 2021a; Zhong et al., 2021b; Feng et al., 2022; Sau et al., 2022; Hatakeyama et al., 2023). The flexibility inherent in AM allows for the design of intricate internal geometries, near-net shapes, and customized components, potentially reducing material waste and manufacturing lead times (Frazier, 2014; DebRoy et al., 2018b; Zhou et al., 2019). Directed Energy Deposition (DED's) capability to repair and clad existing components offers significant advantages for the maintenance and longevity of critical nuclear infrastructure (Saboori et al., 2019; Ahn, 2021; Gradl et al., 2022). Subramaniam Nellian and Hock Lye Pang (2022) demonstrated the use of Laser Metal Deposition (LMD) for repairing rail steel using Stellite six powder, implying the use of additive manufacturing for repair purposes. In another work, Aprilia et al. (2022) et al. focused on the utilization of laser DED for repair application and concluded that Wire-based DED configuration was found to be better suited for repairing large-damaged components, whereas the powder-based DED configuration is ideal for repairing small-damaged components. Svetlizky et al. (2022) emphasized the benefits of DED-based automated repair for complex geometries requiring tight tolerances. In addition, LENS™ technology has achieved Manufacturing Readiness Level (MRL) 10 for repairing H13 tool steel injection molds since 2011 and has been successfully applied to repair T700 jet engine disks and Ti6Al4V airfoil leading edges with Co-based wear-resistant alloys (Martin Hedges, 2006; Liu et al., 2017; Najmon et al., 2019; Svetlizky et al., 2022). The MRL scale (ranging from 1 to 10, with 10 being most mature) is a framework developed by the U.S. Department of Defense to evaluate manufacturing process maturity (Svetlizky et al., 2022).

Addressing the printability challenge in DED requires precise control over the complex interplay between key process parameters primarily–laser power, scan speed and powder feed rate (Dass and Moridi, 2019; Ahn, 2021). Due to the large number of process variables that affect the part's quality, only a few commercial alloys suitable for industrial applications have been successfully manufactured using AM, resulting in a currently negligible market share for these products (Wei et al., 2021). This limited market adoption is primarily due to the high likelihood of defects in AM components, such as lack of fusion, balling, delamination between layers, cracking, and porosity (DebRoy et al., 2018a), along with constraints in powder availability. These defects in general, contribute to the porosity or a lower relative density (Niu et al., 2020; Yang et al., 2021) which affects the quality and reliability of the parts, thereby requiring post-processing to remove defects, adding to the cost of production. Thus, optimization of the process parameters to produce defect free-parts is essential for the wider adoption of AM in the nuclear industry.

Ferritic/Martensitic (F/M) steels are known for their strength, oxidation resistance, and suitability for applications in both fusion and fast fission reactors (Shrestha et al., 2015; Sridharan and Field, 2019a). Additionally, F/M steels have a higher thermal conductivity, lower expansion coefficient, better creep resistance, radiation tolerance, and better void-swelling resistance compared to those of austenitic stainless steels, making them more desirable for in-core applications such as cladding, wrappers, or ducts (Seran et al., 2001; Klueh et al., 2007; Shrestha et al., 2015; Sridharan and Field, 2019a). In addition, Reduced Activation Ferritic-Martensitic (RAFM) steels are widely recognized as superior materials for nuclear systems due to their favorable neutron economy as RAFM steel is considered as the primary structural material for blanket module of nuclear fusion reactors (Huang et al., 2022; Kumar et al., 2022).

F/M steels, including modified Grade-91 (henceforth referred to as G-91) and its variants (P91, P92, NF616), as well as EUROFER and F82H, are regarded as promising structural materials for fast reactors, petrochemical industries, and various advanced nuclear power production applications (Kohyama et al., 1996; Viswanathan and Bakker, 2001; Klueh and Nelson, 2007; Fazio et al., 2009). These materials typically require a combination of high strength, excellent creep resistance, and good ductility. Modified G-91 (9Cr1MoVNb) belongs to the second generation of high-chromium steels designed for high-temperature applications (Guguloth and Roy, 2017). It is well known for its superior resistance to void/cavity swelling under neutron irradiation (Gelles, 1994; Toloczko and Eiholzer, 1994), adequate thermal conductivity, and low thermal expansion coefficients, making it a preferred choice for nuclear reactor components. Currently, G-91 is broadly used in fossil and nuclear power plants in components operating at temperatures up to ~650 °C (Packan et al., 1990). Although several studies have investigated the microstructure of G-91 using laser powder bed fusion (LPBF) both before and after heat treatment, as well as high-temperature tensile testing and creep testing (Eftink et al., 2021b; El-Atwani et al., 2021; Hatakeyama et al., 2023), there has been limited research utilizing powder-based DED to fabricate this alloy and understand its microstructural evolution and mechanical behavior (Zhong et al., 2021b; Samuha et al., 2023a).

One notable limitation of the F/M steels was creep-rupture strengths. Loss of long-term creep rupture strength in G-91 steel was attributed to the nucleation and growth of detrimental phases (Samuha et al., 2023a). Panait et al. (2010) investigated the microstructure of the G-91 steel after more than 100,000 h of creep exposure at 600 C and reported substantial loss of creep strength due to significant precipitation, coarsening of chromium-rich $M_{23}C_6$ type precipitates and Laves phases, and recovering the tempered martensitic lath structure. The positive effects of tungsten (W) and molybdenum (Mo) on creep rupture strength are predominantly attributed to solid solution strengthening. However, the formation and growth of the Laves phase can diminish creep resistance by depleting these elements from the ferrite matrix, thereby negating their strengthening benefits. Despite this, the presence of Laves phase along sub-grain boundaries can enhance creep resistance by restricting deformation at grain and sub-grain boundaries through precipitation hardening (Ennis et al., 1997). Yadav et al. (2018) modelled creep behavior of P91 steel using a hybrid approach that couples a physical model to continuum damage mechanics (CDM) approach and considers dislocation density, sub-grain size and damage evolution during creep exposure. They reported that due to the continuous annihilation of dislocations assisted by glide and climb motion, internal stress decreases and effective stress (resultant of applied stress and internal stress) increases during the creep. They also observed glide velocity to be one order of magnitude higher compared to climb velocity, suggesting glide dominates over climb and accommodates the creep strain.

TABLE 1 Literature on DED process parameters for F/M steels.

Machine	Alloy	Laser power, W	Laser scan speed, mm/s	Hatch spacing, mm	Powder Mass Flow rate (PMFR), g/min	Layer thickness, mm	Laser spot size, mm	Porosity, %	Ref.
DMD 103D system	ANA2	600	10	0.6	6	0.6	1.5	-	Zhong et al. (2021a), Tan et al. (2022b)
2 kW continuous fiber laser	Reduced activation steel	800	6	-	8	0.5	3	-	Xia et al. (2020)
Optomec LENS 850R	Grade 91	400	5	-	2	0.2	1.4	-	Villaret et al. (2021b)
Optomec LENS 500	Fe–9Cr	260/320/380	3/5/7/9/11	0.35–0.71	3.3/6.24/9.3	0.22–1.97	0.7	0.04–13.35	Whitt et al. (2023b)
Optomec LENS MR7	Grade 91	-	-	-	-	-	-	-	Samuha et al. (2023b)
Optomec LENS MR7	AF9628	200/250/ 300/350/400	4.23/6.35 /8.47	0.31–0.87	4.7/6.4/8.2	0.11–0.44	0.6	0.05–0.83	Vaughan et al. (2023)
Modulo 450 by BeAM	Fe–9Cr–2W–V	700	11.7	0.6	6	0.5–0.6		-	Gräning and Sridharan (2022)
DMD 103D System	HT9	-	-	-	-	0.6–0.8	1.5	-	Sridharan et al. (2019b)

In a separate study, Yadav et al. (2016b) modeled the creep behavior of P92 steel up to the onset of the tertiary creep stage using a similar approach. Their findings revealed that during creep, the density of mobile dislocations—responsible for gliding under load—and dipole dislocations—typically forming dipolar or multipolar bundles—decreases, while sub-grains undergo coarsening. Additionally, the density of boundary dislocations, which form sub-grain boundaries arranged in lower-energy configurations, initially increases at the early stages of creep but subsequently decreases as sub-grain growth progresses.

Fournier et al. (2011) investigated high temperature fatigue and creep-fatigue of various 9%–12% Cr steels (P91, P92, 10Cr, 10CrN, 10CrNW) and observed cyclic softening effect for all the materials studied which was attributed to decrease in dislocation density and sub-grain coarsening. Coarsening of precipitates and sub-grains were observed to decrease the creep strength in Grade 91 steel as they become less effective in hindering the movement of mobile dislocations (Sklenicka, 2003; Hald, 2008; Choudhary and Isaac Samuel, 2011; Sawada et al., 2011; Shrestha et al., 2013). Shang et al. (2023) in their investigation of creep behavior in P92 steel under varying stress levels, reported that precipitate size and martensite lath width significantly influenced both the primary and steady-state creep stages. At high applied stresses (>90 MPa), slight coarsening of precipitates and laths occurred, accompanied by the rapid formation of fine dislocation cells within the laths. This accelerated the transition into the steady-state creep stage. In contrast, at low applied stresses (90 MPa), coarsening of $M_{23}C_6$ carbides and Laves phases was observed, and the fine martensite packets or blocks disappeared. This process facilitated dislocation recovery and the formation of new sub-grains within the laths. Consequently, the creep rate declined gradually, leading to the onset of the steady-state creep stage.

In response to these challenges, Grade-92 (henceforth referred to as G-92) steel was developed as a third generation creep-resistant F/M steel with the addition of tungsten and reduction of Mo content (Tan et al., 2022a) to improve the creep properties of second generation of G-91 steel. Despite efforts to design thermally stable precipitates for enhancing the creep strength of 9Cr tempered martensitic steels (Abe, 2008), it has not yet been code-qualified. Currently, to the best of the authors' knowledge, there is no existing research on the additive manufacturing of G-92 steel.

Even though conventional manufacturing of P91 and P92 is well understood, that is a reason for it to be evaluated for additive manufacturing. The nuclear industry's heavy regulation requires that materials be well understood prior to use in reactor components. The increased complexity of next-generation reactors further increases the attractiveness of utilizing additive manufacturing over conventional manufacturing techniques. Previous AM research has predominantly focused on conventional stainless-steel alloys, such as grade types 304 and 316. With growing interest in applying metal AM to next-generation nuclear reactors, this study compiles and examines a range of process parameters from existing literature relevant to the AM fabrication of G-91 and G-92 steels. The limited publications on DED of F/M steels and the associated process parameters are outlined in Table 1.

A key consideration for (F/M) steels is the martensite start (M_s) temperature, which is primarily influenced by the Mn content (Zhong et al., 2021c), along with Cr, Mo, Si, and C contents. In general, higher concentrations of these elements tend to lower the M_s temperature. The influence of Mn, Si, and Al content on the M_s temperature is linear, with increasing Mn and Si content leading to a gradual decrease in M_s temperature, whereas adding Al content increases in M_s temperature (Kaar et al., 2021). Additionally, the inclusion of several ppm of C significantly reduced the M_s temperature (Tsuchiya et al., 1965; Kaar et al., 2021). Kaar et al. (2021) introduced a new M_s relation by incorporating the non-linear effects of both C and N content. They compared this with various M_s formulas available in the literature, which yielded the highest correlation coefficient (R^2). An elevated M_s temperature can result in increased tensile residual stresses, thereby enhancing the brittleness of the alloy (Zhong et al., 2021a). Brittleness is of great concern during fabrication with DED processes due to the large thermal gradients and rapid cooling and solidification associated with the AM process. An aspect of the methodology for process parameter selection in this study was a qualitative comparison of the above elements to determine whether M_s temperature was improved compared to the relevant publications. G-91 steel has higher content of Mn, Si, and N combined, while G-92 steel has higher contents of C and N, both of which can potentially reduce the M_s temperature compared to Fe–9Cr (wt%) (Whitt et al., 2023a) and Fe–9Cr–2W–0.25V (wt%) (Gräning and Sridharan, 2022). Consequently, G-91, and G-92 are expected to be less brittle than Fe–9Cr (wt%), and Fe–9Cr–2W–0.25V (wt%) under the same process parameters. The other alloys listed in Table 1 have similar or identical compositions compared to those of the G-91 and G-92 steels, and all research reported success with the selected process parameters. The process parameters for this work were selected from the ranges of values listed in Table 1.

The purpose of this study is the development of DED process parameters for G-91, and G-92 steels, followed by preliminary microstructural characterization, and micro-hardness evaluation. $10 \times 10 \times 12$ mm^3 blocks were produced with a wide range of laser powers and scan speeds, to optimize the build quality. The microstructure, phase constituents, and mechanical properties were analyzed using electron microscopy, powder X-ray diffraction, and Vickers hardness testing, respectively.

2 Materials and methods

2.1 DED of G-91, and G-92 steel

Based on the literature data and discussion in the previous section, it was determined that the optimal process parameter overlapped for the G-91 and G-92 steel. As such, a single range of process parameters was selected for use for both alloys. However, it is important to highlight that variability among different original equipment manufacturers (OEMs) can result in inconsistent quality and performance of printed parts.

Commercial G-91, and G-92 steel powders were acquired from Linde Advanced Material Technologies Inc. (Indianapolis, IN). Powder particle sizes were in the range of 50–150 μm. The powders were mostly spherical in shape with the presence of some satellites. Secondary electron micrographs of G-91, and G-92 powders are presented in Figures 1a,b, respectively. The primary difference between G-91 and G-92 is that the latter has additional tungsten (W) and reduced Mo content. The manufacturers reported powder chemistry and SEM-EDS composition for both the alloys are presented in Table 2.

FormAlloy DED L2 Additive Manufacturing System was utilized to produce the G-91, and G-92 blocks for an optimization study. The FormAlloy DED L2 system is equipped with a 1 kW continuous-wave (1064 nm wavelength) yttrium aluminum garnet (YAG) laser with a spot size of ~1.2 mm. Blocks with a dimension of $10 \times 10 \times 12$ mm^3 as presented in Figures 1c,d were built with various laser powers (400–800 W), scan speeds (600–900 mm/min), hatch spacings of 0.9 mm, layer height of 0.325 mm, and scan rotation of 90°. The powder feed rate was fixed at one revolution per minute (rpm) equating to ~5 g/min. The deposition process was carried out within a controlled atmosphere chamber, purged with argon gas to maintain an oxygen level below 50 ppm. Additionally, two samples with the same thickness (0.53 mm) were deposited with a laser power of 400W and 800W and the same scan speed (600 mm/min) for both the alloys. These depositions were done to understand the effect of the layer thickness setting on deposition characteristics in DED process of this alloy. Employing a fixed-thickness setting during DED fabrication typically decreases the geometrical accuracy of a part, primarily due to the relationship between deposited layer height and instantaneous laser power and scan speed at the respective location. Hence, a study on the impact of the fixed-thickness setting procedure was proposed that allows the slice thickness to be adapted as a function of both the actual deposited height and the process conditions.

2.2 Characterization methods

In preparation for microstructural characterization, the G-91 and G-92 alloy samples were sectioned into XZ cross-sections. Each sectioned sample was mounted in epoxy and prepared metallographically with grinding and polishing. All samples were given a final polish using 1 μm diamond polishing paste and a colloidal silica (0.05 μm) polishing suspension. Once the final polishing was completed, samples were examined using an Olympus DSX510 metallurgical microscope. Five micrographs were taken for each sample and were processed with a thresholding technique to determine flaws (porosity) utilizing the ImageJ software (Abràmoff et al., 2004). The process involved converting unetched micrographs to 8-bit images to reduce the signal-to-noise ratio, followed by applying the color threshold function to convert the images to black-and-white. The pixel fraction corresponding to pores/flaws was then calculated and used to determine density via image analysis.

Additionally, the Archimedes density of two G-91 and G-92 steel samples was measured following the ASTM B311 standard (Bruce et al., 2022) for greater accuracy. For statistical significance, measurements were conducted using n = 10 data sets. One sample had the lowest laser power and scan speed (400 W, 500 mm/min), while the other was fabricated using a laser power of 500 W and scan speed of 700 mm/min, which were the same process parameters used for fabricating the large cylinders.

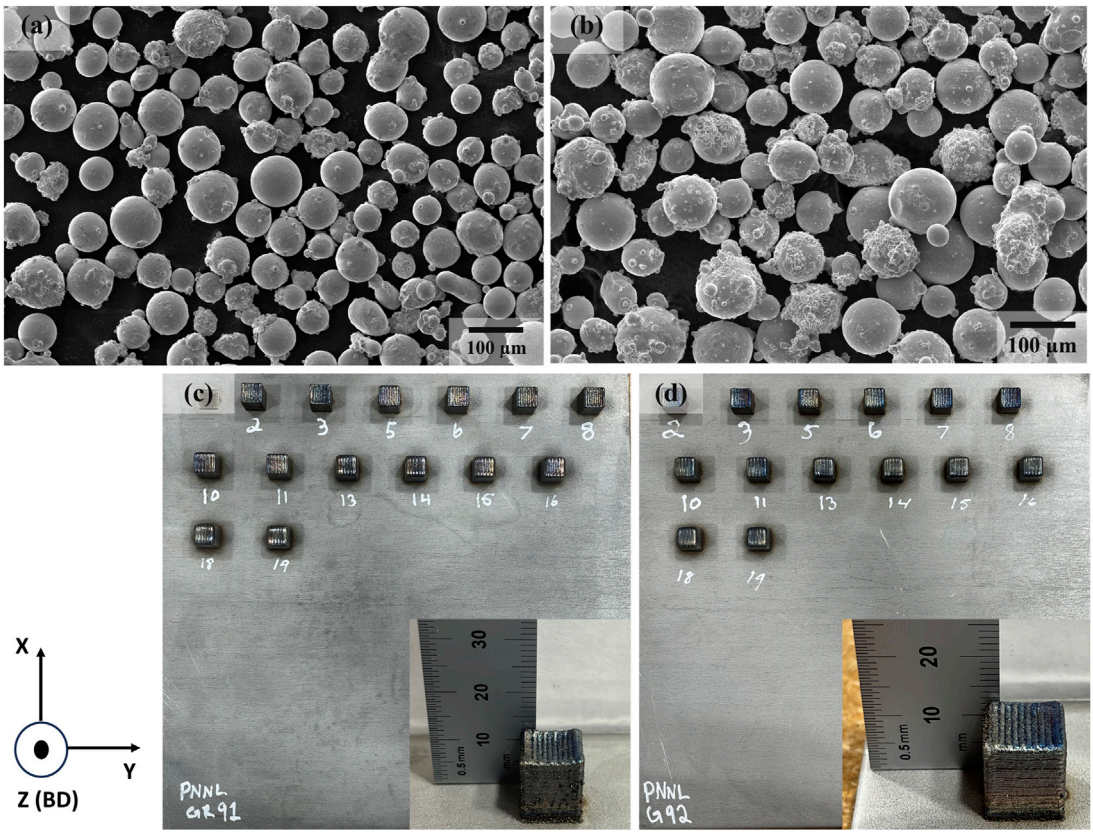

FIGURE 1
Secondary electron micrographs of powders and macrophotograph of DED-fabricated blocks: **(a)** G-91 powders, **(b)** G-92 powders, **(c)** G-91 blocks, and **(d)** G-92 blocks. The coordinate system shown is applicable exclusively to the printed blocks shown in Figures 1C,D.

TABLE 2 Manufacturers reported powder chemistry data (wt%) and EDS composition for G-91 and G-92 steel. C and N were excluded during the EDS analysis for the G-91 and G-92 blocks.

	C	Cr	Fe	Mn	Mo	N	Nb	Si	V	W
Powder G-91	0.07	8.5	Bal	0.4	0.94	0.06	0.07	0.3	0.19	0
DED G-91	-	9.36	Bal	0.48	0.93	-	0.07	0.32	0.22	0
Powder G-92	0.09	8.8	Bal	0.4	0.4	0.09	0.08	0	0.19	1.7
DED G-92	-	9.39	Bal	0.51	0.46	-	0.04	0	0.21	1.67

TABLE 3 Archimedes density and relative density of selected samples. Theoretical density values were taken from literature (Wang et al., 2016a; Taler et al., 2017).

Sample ID	Archimedes density (g/cm^3)	Theoretical density, (g/cm^3)	Relative density (%)
G-91: 400W, 500 mm/min	7.72 ± 0.01	7.75	99.613 ± 0.129
G-91: 500W, 700 mm/min	7.761 ± 0.007	7.75	100.142 ± 0.09
G-92: 400W, 500 mm/min	7.833 ± 0.009	7.85	99.783 ± 0.115
G-92: 500W, 700 mm/min	7.845 ± 0.005	7.85	99.936 ± 0.064

Theoretical density values were taken from literature: G-91 density was assumed to be similar to P91 steel (Taler et al., 2017) while the theoretical density of G-92 was based on (Wang et al., 2016a). Relative density was then calculated using Equation 1, and both measured Archimedes density and relative density values are presented in Table 3.

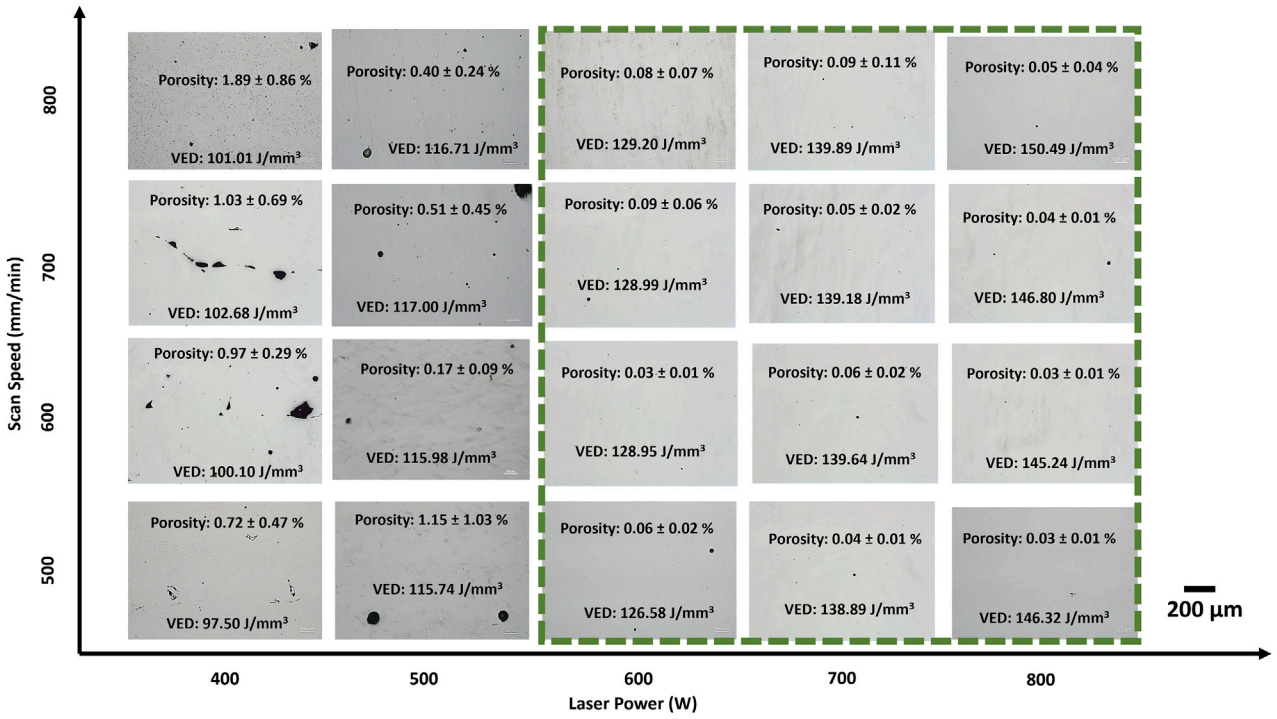

FIGURE 2
Optical micrographs of XZ cross sections of G-91 samples produced with various laser powers and laser scan speeds.

$$\text{Relative Density, } (\%) = \frac{\text{Archimedes Density } \left(\frac{\text{g}}{\text{cm}^3}\right)}{\text{Theoretical Density } \left(\frac{\text{g}}{\text{cm}^3}\right)} \times 100 \qquad (1)$$

An FEI Helios 660 Nanolab dual-beam focused ion beam (FIB) scanning electron microscope (SEM) equipped with XEDS was used to examine the cross-sectional phase constituents, microstructures, and composition of the G-91 and G-92 samples. Grain orientation mapping with a step size of 50 nm was performed using a JEOL IT800 FESEM equipped with an Oxford Instruments Symmetry EBSD detector. Oxford Instruments AZtec Nanoanalysis v.4.3 was used for data acquisition in conjunction with AZtec Crystal v.3.3 for EBSD post processing and analysis. The 15° misorientation criterion was used to distinguish the low angle grain boundaries (LAGBs) and high angle grain boundaries (HAGBs) (Cui et al., 2021). A 3 × 3 kernel with a threshold of 3° was used to process the kernel average misorientation (KAM) and Geometrically Necessary dislocation (GND) density maps. A detailed description of the KAM and GND density calculation can be found in (Pantleon, 2008; Konijnenberg et al., 2015; Moussa et al., 2015).

A D6 Phaser (Bruker Inc.) powder diffractometer was used to collect X-ray diffraction (XRD) patterns of the samples. The D6 Phaser is equipped with a theta/theta goniometer with a radius of 166.5 mm, Cu Kα radiation, and a 1.2 kW X-ray power generator. All XRD patterns were collected using 0.01° 2θ step size at 0.32 s per step over a 2θ range of 10°–120°.

Vickers microhardness measurements were performed using a Sun-Tec (model: CM-802 AT) microhardness tester, operated with the ARS20 software for automated measurements. A load force of 300 g-force was applied for a duration of 10 s for each indentation. An array of 2 × 20 indentations was performed on each sample, each indentation separated by 0.5 mm. This spacing ensures that measurements were not influenced by neighboring indentations, providing reliable and repeatable hardness values. Calibration checks were conducted using Sun-Tec calibration standards (249HV0.3 and 297HV0.3) to verify that the instrument was calibrated. These checks confirmed that the hardness values measured were within ±2% of the calibration standard, ensuring the accuracy of the measurements.

3 Results

3.1 G-91 steel

3.1.1 Microstructure and phase constituents of G-91 steel

Figure 2 shows optical micrographs of the XZ cross-sections of G-91 samples produced using various laser powers and scan speeds. The micrographs revealed that samples produced with low laser power exhibited a high density of defects, primarily lack of fusion flaws, along with some keyhole pores and gas-entrapped porosity. In contrast, samples produced with high laser power regardless of scan speed showed no significant defects. The optimal processing window for G-91 steel, highlighted in green in Figure 2, was identified as laser power ranging from 600 to 800 W and scan speed from 500 to 800 mm/min, with a constant hatch spacing of 0.9 mm and a layer height of 0.325 mm based on porosity analysis using ImageJ. Volumetric energy density (VED) was calculated using

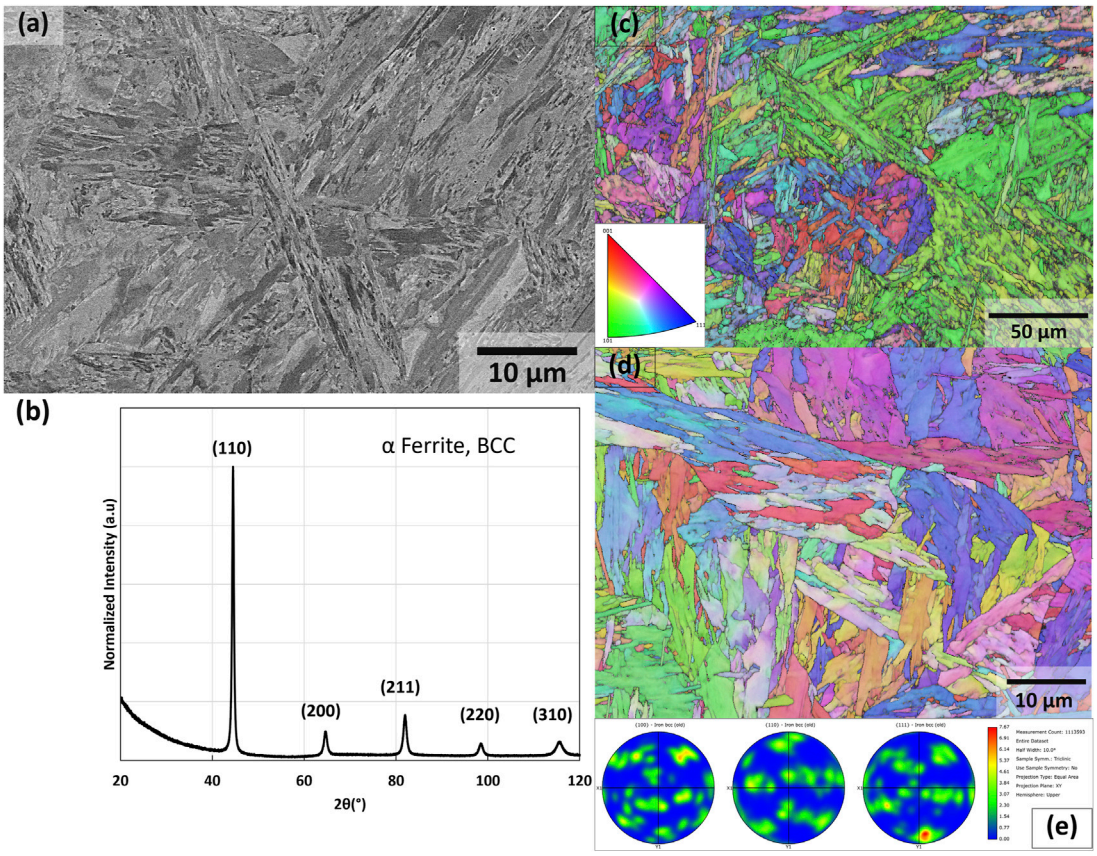

FIGURE 3
Microstructure and phase constituents of G-91 steel: **(a)** BSE micrograph, **(b)** Representative XRD pattern **(c)** EBSD IPF maps at low magnification, **(d)** EBSD IPF maps at high magnification, and **(e)** pole figures, all obtained from XZ cross sections.

Equation 2 (Ciurana et al., 2013; Scipioni Bertoli et al., 2017; Eliasu et al., 2021):

$$\mathrm{VED}\left(\mathrm{J/mm^3}\right) = \frac{\text{Laser power (W)}}{\text{Laser scan speed}\left(\frac{\text{mm}}{\text{s}}\right) \times \text{hatch spacing (mm)} \times \text{layer thickness (mm)}} \quad (2)$$

Representative backscattered electron micrograph (BSE) of G-91 steel is presented in Figure 3a. The microstructure primarily consisted of fine and coarse lath martensite and average width of the laths were measured to be 3.28 ± 0.78 µm. Eftink et al. (2021b) examined the microstructure of G-91 steel produced via LPBF and reported that the as-deposited G-91 steel had a microstructure of lower bainitic regions surrounded by martensite. They also found that the as-deposited microstructure of G-91 steel consisted of three regions: areas of uniform dislocation and platelet distribution (lower Bainite), a similar region of uniform dislocations and platelets with finer grain sizes, and martensitic regions characterized by high strain and laths. Samuha et al. (2023a) reported the fabrication of G-91 steel via DED and found that the majority of the microstructure consisted of fine and coarse-sized lath-type martensite grains, with up to 15% δ-ferrite phase, predominantly located at melt pool boundaries.

Figure 3b illustrates the representative XRD pattern obtained from G-91 steel. The XRD pattern showed strong reflections from body-centered cubic (BCC) α-ferrite. Robin et al. (2024) reported a high density of dislocations in wire arc-based AM (WAAM) G-91 resulting in a large amount of microstrain and the presence of martensite phase buried under the BCC peaks. Synchrotron X-ray diffraction analysis of as-deposited G-91 steel produced via LPBF indicated that the BCT martensite phase constitutes approximately 15% of the volume fraction (Eftink et al., 2021b).

Figures 3c,d present the electron backscattered diffraction (EBSD) inverse pole figure (IPF) mapping at low and high magnifications, respectively, along with pole figures of G-91 (Figure 3e) steel showing crystallographic texture. It is important to note that the low-magnification EBSD IPF maps were taken with a different machine and with a slightly different step size. The KAM, GND, and pole figures were all derived from the high-magnification EBSD IPF maps.

KAM generally serves as an indicator of local lattice curvature and is defined as the average misorientation between a kernel point and its neighboring points, excluding those beyond the grain boundary. Generally, higher KAM values indicate severe deformation, which is associated with an increased dislocation density (Rui et al., 2021). Figure 4 presents the KAM map of G-91 steel acquired from the EBSD data with an area roughly $80 \times 80\ \mu m$ and with an indexing rate of above 93% and step size of 50 nm. The average KAM value for G-91 steel was found to be 0.39° ± 0.21°.

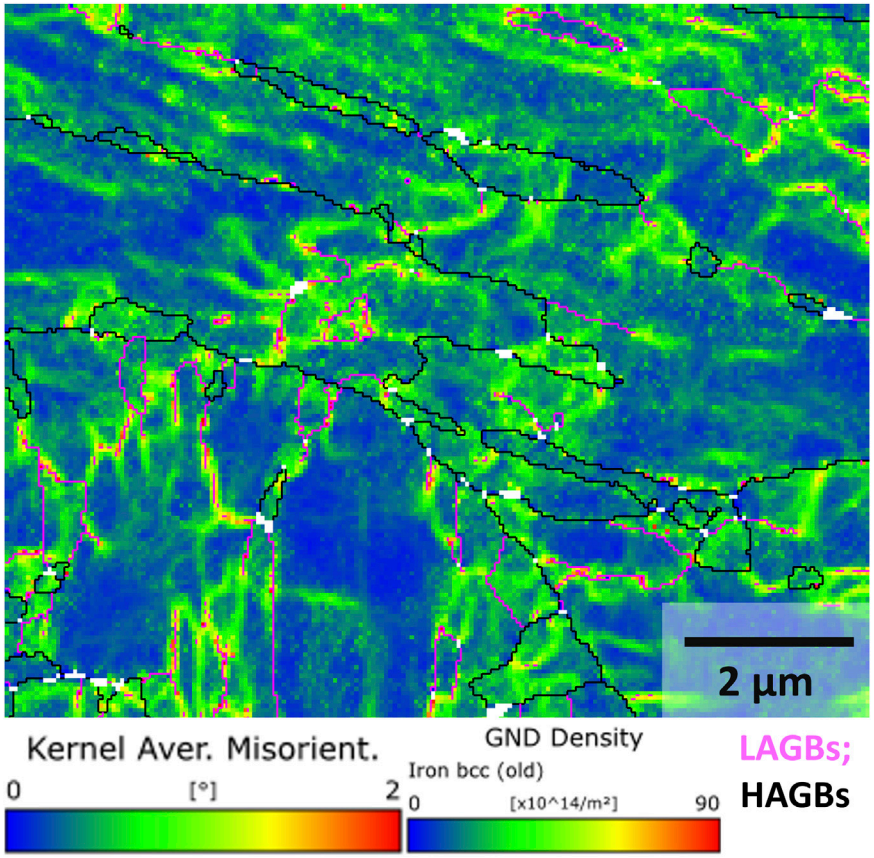

FIGURE 4
Kernel average misorientation (KAM) and geometrically necessary dislocation (GND) density maps of G-91 steel calculated from EBSD acquired data. LAGBs were marked lavender while HAGBs were marked black and the 15° misorientation criterion was used to differentiate the LAGBs and HAGBs. A 3 × 3 kernel with a threshold of 3° was utilized to process both the KAM and GND density maps.

Local misorientations are usually caused by the curvature of the crystal lattice associated with geometrically necessary dislocations (GNDs) and the impact of the elastic strain field. However, the influence of the elastic strain field is generally minimal, allowing it to be considered negligible, thus attributing lattice curvature primarily to the presence of GNDs (Wilkinson and Randman, 2010). For qualitative analysis of geometrically necessary dislocations (GNDs) using EBSD data, two methods are commonly employed: the first involves calculating the dislocation density tensor as proposed by Nye (1953), while the second estimates the GND density based on the misorientation angle between measurement points separated by a given distance x (Gao et al., 1999; Kubin and Mortensen, 2003). Equation 3 is generally used to express the relationship between GND and misorientation angle θ:

$$\rho_{GND} = \frac{\alpha\theta}{bx} \tag{3}$$

where θ is the threshold disorientation angle, b is the burgers vector, x is the acquisition step size, and α is a constant ranging from 2 to 5.1 where α equals two for pure tilt boundary, three for strongly textured disorientation axes, four for pure twist boundaries, and 5.1 for random disorientation axes (Konijnenberg et al., 2015; Moussa et al., 2015; 2017; Sow et al., 2020; De Terris et al., 2021).

AZtecCrystal (version 3.3) was utilized to map Kernel Average Misorientation (KAM) and GND distribution by analyzing in-grain orientation gradients following the method outlined here (Moussa et al., 2017; Sow et al., 2020; De Terris et al., 2021). This technique involves calculating the misorientation between adjacent EBSD pixels as a function of the distance between them, addressing measurement noise and the spacing between EBSD points (steps). In this study, GND density maps were calculated from EBSD acquired data with an area roughly 80 × 80 μm and with an indexing rate of above 93% and step size of 50 nm as presented in Figure 4. The bright colors (red and orange) in Figure 4 corresponds to high dislocation density (dislocation walls) while dark color (blue) corresponds to low dislocation density. The GNDs were observed to be heterogeneously distributed across the microstructure and typically located along the LAGBs (Cui et al., 2021). The average GND density of as-deposited G-91 produced via laser powder DED was determined to be (16.06 ± 8.71) × 10^{14}/m^2. G-91 steel, in its undeformed state, typically exhibits a dislocation density of approximately 1 × 10^{14} m^{-2}, which was attributed to its tempered martensitic structure (Wang et al., 2014; Laliberte et al., 2018).

3.1.2 Vickers Hardness of G-91 steel

Figure 5 presents the representative Vickers hardness of G-91 steel. Two arrays of indents L1, and L2 were performed on the

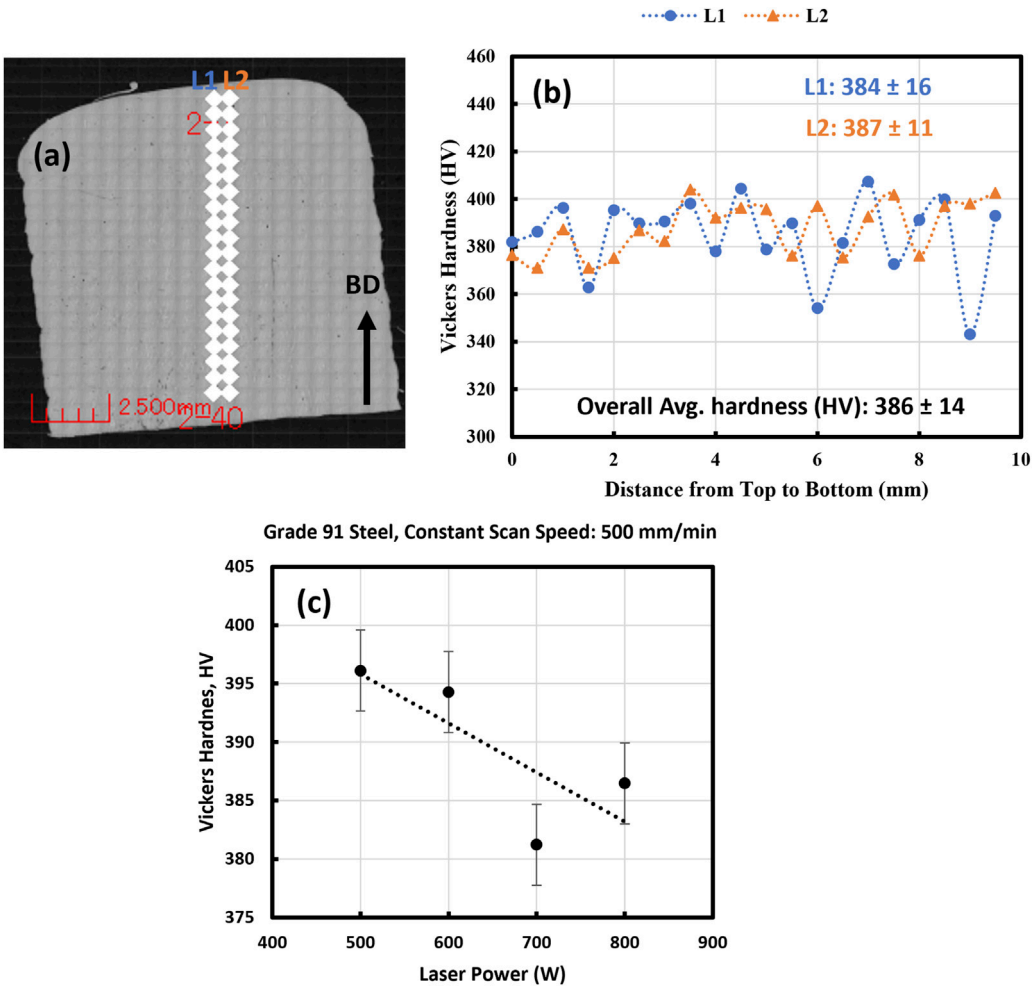

FIGURE 5
Representative Vickers hardness of G-91 steel: **(a)** optical micrograph with two arrays of indents (spacing between indents: 0.5 mm) L1, and L2 respectively, **(b)** Vickers hardness as a function of indents, and **(c)** Variation in Vickers hardness with laser power at a constant scan speed of 500 mm/min. The indentation patterns are schematic and not drawn to scale.

sample to measure the variation in hardness from top to bottom of the produced 10 × 10 × 12 mm^3 block as shown in Figure 5a. L1 showed a slight variation in hardness compared to L2, however, no significant differences were observed between the average Vickers hardness of L1 and L2. Figure 5c presents the variation in the Vickers hardness with the change in the laser power (500 W–800 W) while the laser scan speed was kept constant at 500 mm/min for the G-91 samples. It was observed that, in general, the Vickers hardness decreased with an increase in laser power. This decline could be attributed to a corresponding increase in grain size at higher laser power inputs.

3.2 G-92 steel

3.2.1 Microstructure and phase constituents of G-92 steel

Optical micrographs of the XZ cross section of G-92 samples produced with various laser powers and laser scan speeds are presented in Figure 6. The optical micrographs revealed that samples produced at a low laser power exhibited a high density of defects, primarily lack of fusion flaws while the samples produced at a high laser power regardless of scan speed showed no significant defects. The optimal processing conditions for G-92 steel, highlighted green in Figure 6, were identified as a laser power range of 500 W–800 W and a scan speed range of 500 mm/min to 800 mm/min based on porosity analysis using ImageJ. However, the sample produced with 500W, and 500 mm/min showed significant lack of fusion flaws. A hatch spacing of 0.9 mm, a layer height of 0.325 mm, and a powder feed rate of 1 rpm were kept constant. The representative BSE micrograph of G-92 steel is presented in Figure 7a. The microstructure primarily consisted of fine and coarse lath martensite and average lath width were measured to be of 3.17 ± 1.50 μm. Ennis et al. (1997) reported that in P92 steel austenitized at 1000 °C, the average sub-grain width (formed by original martensite lath boundaries) increased from 0.37 μm to 0.50 μm as the tempering temperature was raised from 715 °C to 835 °C, indicating that higher tempering temperatures promote larger sub-grain structures. Yadav et al. (2016a) studied a novel 12% Cr martensitic/ferritic steel alloyed with Ta and observed

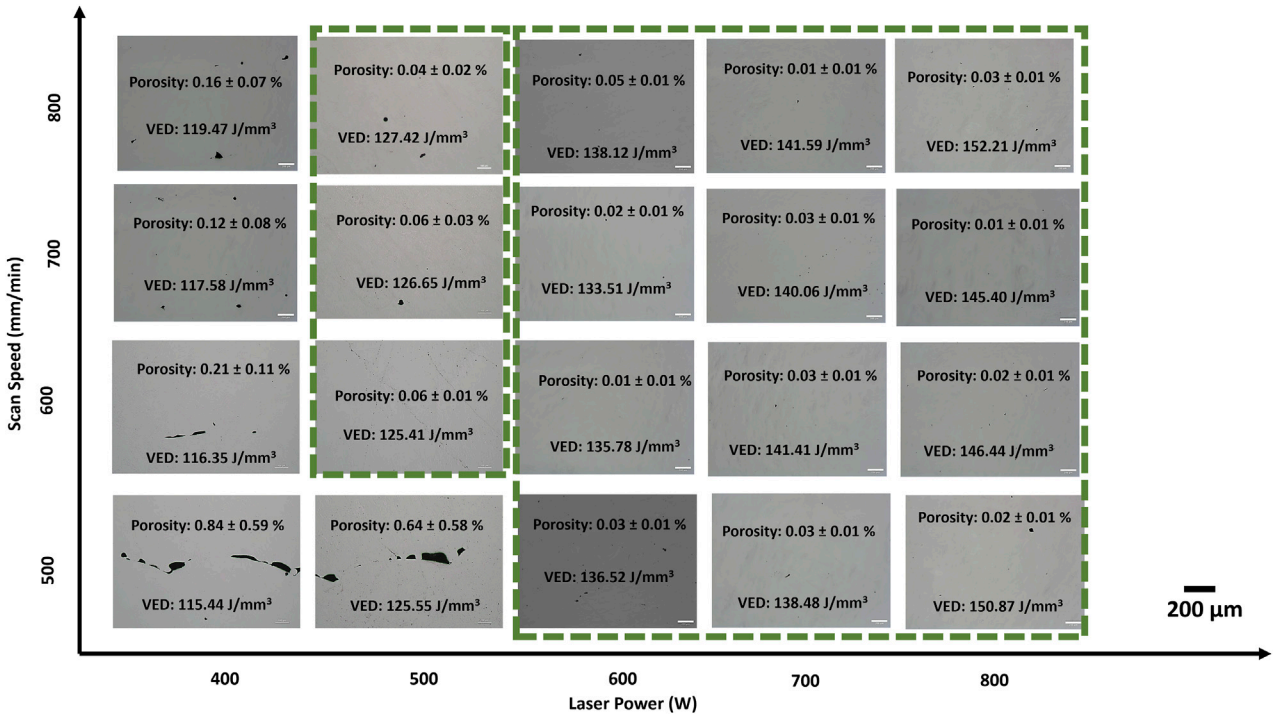

FIGURE 6
Optical micrographs of the XZ cross sections of G-92 samples produced with various laser powers and laser scan speeds.

a sub-grain size of 0.52 µm in the as-received condition. Additionally, the mean prior austenite grain size in Grade 91 steel (Sawada et al., 2011) was reported to be approximately 10 µm, while the mean sub-grain size for 12Cr1MoV, P91, and P92 steels ranged between 0.35 and 0.42 µm (Shrestha et al., 2013).

Figure 7b presents the representative XRD pattern collected from G-92 steel. The XRD pattern showed strong reflections from BCC α-ferrite. Like the G-91 steel, the martensite phase was assumed to be buried under the BCC peaks. Figures 7c,d present the EBSD IPF maps at low and high magnifications, respectively, along with the pole figures of G-92 steel (Figure 7e) showing its crystallographic texture. It is important to note that the low-magnification EBSD IPF maps were taken with a different machine and with a slightly different step size. The KAM, GND, and pole figures were all derived from the high-magnification EBSD IPF maps.

Similar to G-91, KAM and GND density maps of G-92 steel were calculated from EBSD acquired data with an area roughly 80 × 80 μm, indexing rate of above 93% and step size of 50 nm as presented in Figure 8. The bright colors (red and orange) in Figure 8 correspond to high dislocation density (dislocation walls) while dark color (blue) corresponds to low dislocation density. The GNDs were observed to be heterogeneously distributed across the microstructure with an average GND density of (17.04 ± 9.35) × $10^{14}/m^2$ and, an average KAM value of 0.41° ± 0.24° for G-92 steel.

To investigate the variation in microstructure along the build direction of G-92 steel, a cylindrical rod (L: ~90 mm, diameter: ~13 mm) was fabricated using a laser power of 500 W, a scan speed of 700 mm/min, a hatch spacing of 0.9 mm, a layer height of 0.325 mm, and a powder feed rate of 1 rpm and the microstructure at three different locations was studied. In addition, a 4 × 4 array of indentations, each spaced 0.5 mm apart with a load of 300 gf were performed to assess the variation in Vickers hardness. Overall, no significant differences in microstructures or Vickers hardness were observed at those locations, implying consistent microstructure along the build direction for the G-92 steel as presented in Figure 9.

3.2.2 Vickers Hardness of G-92 steel

Figure 10 presents the representative Vickers hardness of G-92 steel. Two arrays of indents L1, and L2 were performed on the sample to measure the variation in hardness from the top to the bottom of the produced 10 × 10 × 12 mm^3 block as shown in Figure 10a. L2 showed a slight variation in hardness compared to L1, however, no significant differences were observed between the average Vickers hardness of L1 and L2. Figure 10c presents the variation in the Vickers hardness with the change in the laser power (500 W–800 W) while the laser scan speed was kept constant at 500 mm/min for the Grade 92 samples. In general, the Vickers hardness was observed to decrease as the laser power was increased, with a slight deviation at 600 W.

4 Discussion

The G-91 and G-92 samples were produced by varying the laser power and scan speed, while keeping the powder feed rate, hatch spacing, and layer thickness constant. This approach enabled the isolation of the influence of laser processing parameters on part density. Careful selection of these parameters is what resulted in some of the specimens to be nearly fully dense. AM parts are prone to significant failure if the porosity content is not substantially

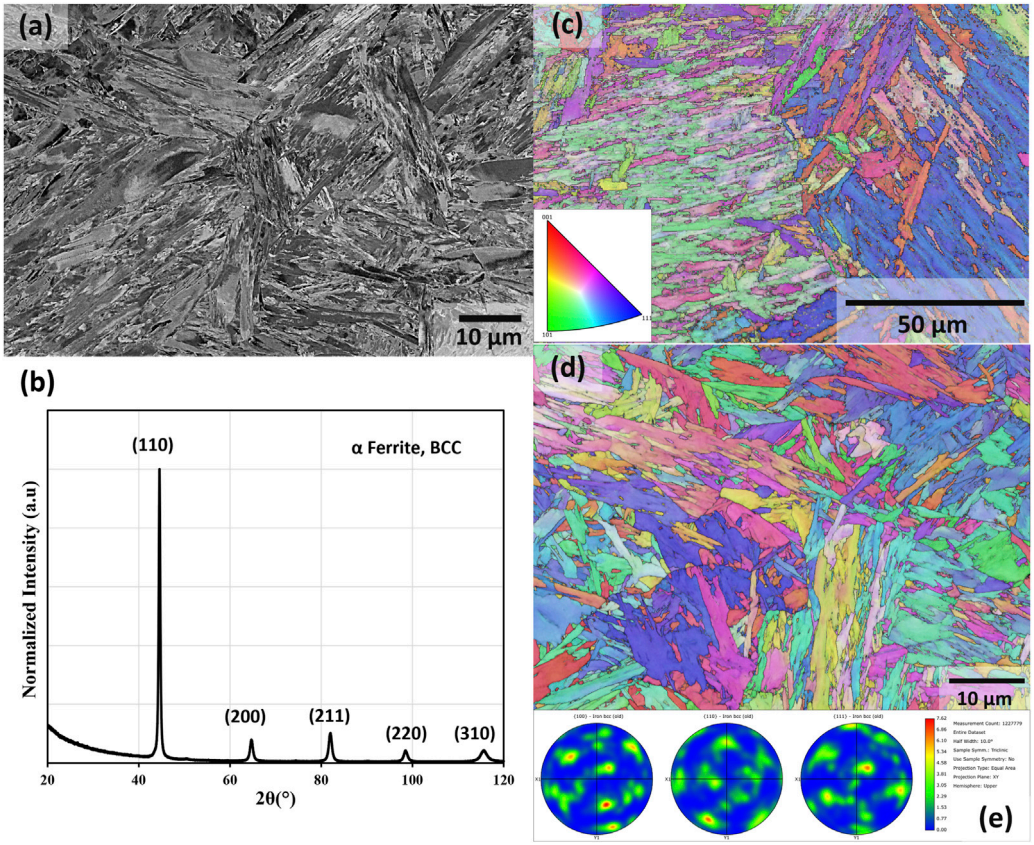

FIGURE 7
Microstructure and phase constituents of G-92 steel: **(a)** BSE micrograph, **(b)** Representative XRD pattern **(c)** EBSD IPF maps at low magnification, **(d)** EBSD IPF maps at high magnification, and **(e)** pole figures, all obtained from XZ cross sections.

reduced, as clusters of pores weaken the material (Demeneghi et al., 2025). Higher laser power and lower scanning speeds introduce more energy into the melt pool, resulting in higher peak temperatures and slower cooling rates. This condition tends to promote better fusion and reduced porosity. However, doing so may pose a risk in inducing keyhole effects. Conversely, lower laser power and higher scanning speeds lead to reduced heat input and faster cooling, which may produce finer microstructures. However, this may increase the challenge of insufficient melting and lack of fusion defects. The work of Dass and Moridi (2019) provides a useful framework for understanding these phenomena by identifying three non-optimal zones based on linear heat input and powder feed rate: (1) the keyhole zone (high heat input, low feed rate), (2) the lack of fusion zone (low heat input, high feed rate), and (3) the mid-porosity zone (high heat input, high feed rate). In this study, by maintaining the powder feed rate at 1 rpm, the risk of defects typically associated with low feed rates in the keyhole regime were effectively minimized. Notably, no significant defects were observed in samples produced at higher laser powers, regardless of scan speed, which indicates a robust processing window for these alloys under the conditions tested. Examination of three different locations along the build direction of the G-92 cylindrical rod revealed a consistent microstructure, and Vickers hardness underscoring the effectiveness of the chosen parameters in controlling solidification dynamics throughout the build.

Busby et al. (2005) developed a correlation between yield strength (σ_y) and Vickers hardness (HV) for ferritic steels, expressed as $\Delta\sigma_y = 3.06\,\Delta H_V$ with an R^2 of 0.90. Yano et al. (2016) studied the tensile properties and hardness of two types of 11Cr-F/M steel after aging up to 45000h and showed a linear relationship between Vickers hardness, yield strength, and ultimate tensile strength. The linear relationship between (σ_y) and HV is as follows (Yano et al., 2016):

$$\sigma_y = 3.39 \times HV - 246.02 \tag{4}$$

where σ is in MPa and HV in kg/mm^2. Equation 4 was employed to estimate the yield strength (σ_y) of as-deposited G91, and G92 steel produced via DED in this study. Table 4 includes Vickers Hardness, estimated σ_y from Vickers Hardness using Equation 4, and the reported σ_y from tensile testing for G-91, and G-92 Steels manufactured via different AM processes. In addition, yield strength values for conventional P91 and P92 steels from literature are included in Table 4 to provide a comparison. Notably, the predicted yield strength of the materials in this study was found to be higher than that of conventional P91 and P92 steels.

Samuha et al. (2023a) reported an average Vickers hardness of 349 ± 21 HV for G-91 stainless steel produced using the DED laser technique. In this study, G-91 samples manufactured with optimal parameters exhibited a hardness of 386 ± 14 HV, which is

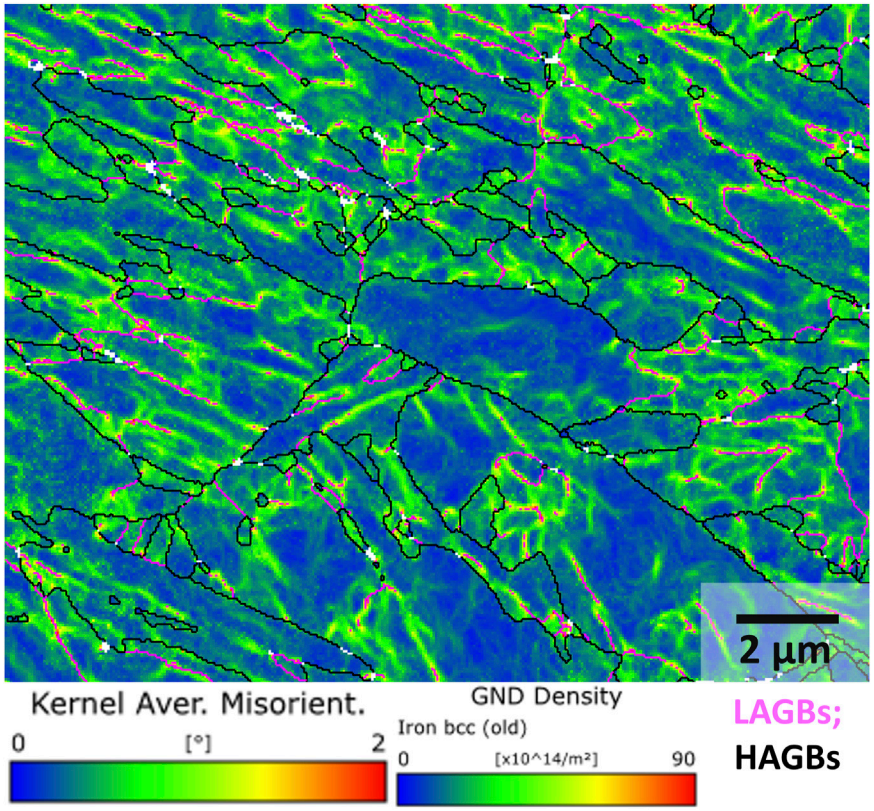

FIGURE 8
Kernel average misorientation (KAM) and geometrically necessary dislocation (GND) density maps of G-92 steel calculated from EBSD acquired data. LAGBs were marked lavender while HAGBs were marked black and the 15° misorientation criterion was used to differentiate the LAGBs and HAGBs. A 3 × 3 kernel with a threshold of 3° was utilized to process both the KAM and GND density maps.

significantly higher than the hardness of wrought normalized and tempered T91 and G-91 steel (260–270 HV) (Zhang et al., 2008; Liu et al., 2015) and higher than that reported by Samuha et al. (2023a).While the enhanced hardness in our study is likely due to the high cooling rate intrinsic to the process, dislocation density, and fine martensite laths, it is important to acknowledge that other factors may also play a role. These factors could include subtle differences in alloy composition, variations in processing parameters beyond those explicitly controlled, or the presence of residual stresses introduced during the rapid solidification process. The slightly higher hardness of G-92 steel may be plausibly attributed to its marginally higher carbon content, addition of W, and higher GND density compared to G-91. The GND density of G-92 was found to be $17.04 \times 10^{14}/m^2$ with an average KAM value of $0.41^{\circ} \pm 0.24^{\circ}$ while GND density of G-91 was observed to be $16.06 \times 10^{14}/m^2$ with an average KAM value of $0.39^{\circ} \pm 0.21^{\circ}$.

Abe and Nakazawa (1992) investigated the effect of W on the creep behavior and microstructural evolution of martensitic 9Cr steel (quenched and tempered) by varying W (0-4 wt%) concentration at 823, 873, and 923K for 15,000 h. The microstructure of 9Cr, 9Cr-1W, and 9Cr-2W steels were composed entirely of tempered martensite, while 9Cr-4W steel exhibited 10 vol% δ-ferrite within the tempered martensite. The martensite lath microstructure with fine carbides distributed along the lath boundaries was observed to be critical for providing high resistance to creep deformation. The addition of W to 9Cr steel was found to reduce the self-diffusion rate as well as the microstructural evolution rate (such as the recovery of dislocations, the agglomeration of carbides, and the growth of martensite lath sub-grains) in the tempered martensite, by reducing the dislocation velocity which in turn decreased the minimum creep rate.

Radiation-induced void swelling is a critical degradation mechanism in nuclear structural materials (Murty and Charit, 2008). Gelles (1994) conducted an extensive study on nine reduced-activation ferritic steels containing 2.3%–12% Cr with varying additions of V and W, irradiated at 420 °C to doses of up to 200 dpa. The results demonstrated that void swelling in these steels remained below 5%, even under high neutron exposure. Similarly, irradiation studies (Toloczko et al., 1994) on HT9 and 9Cr-1Mo steels at dpa levels as high as 208 dpa at ~400 °C reinforced the inherent swelling resistance of this class of steels, although it was noted that high stress levels could accelerate swelling to some extent.

In general, high swelling resistance of F/M steels is attributed to low dislocation bias, high self-diffusion rates, high sub-grain boundary sink strengths and solute atom point defect trapping effect (Odette, 1988; Little, 1993). A high density of carbides typically creates a significant number of coherent interfaces, which act as effective traps for vacancies and interstitials. These traps promote the recombination of radiation-induced defects, thereby reducing void swelling. This mechanism is analogous to oxide dispersion strengthened (ODS) steels, where the introduction of a high density of oxide particles during sample

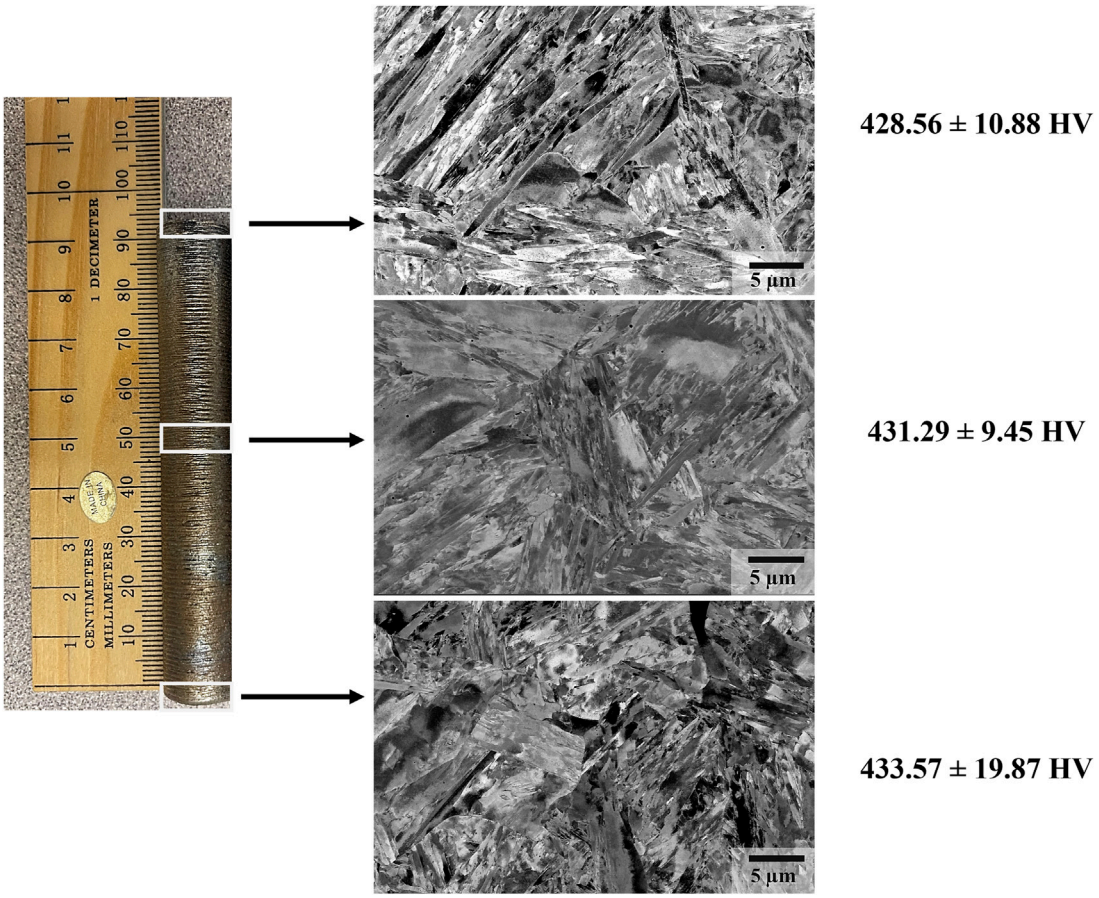

FIGURE 9
Microstructure and Vickers Hardness of G-92 cylindrical rod at three different locations along the build direction.

fabrication serves as defect traps to mitigate swelling (Odette et al., 2008; Wang et al., 2016b).

More recent findings by Wang et al. (2016b) investigated ion irradiation on reduced-activation ferritic-martensitic steels CNS (China Nuclear Steel) I (9Cr, fully tempered martensite) and CNS II (12Cr, tempered martensite and <5% ferrite) up to 375 dpa and 450 dpa at 460 C with pre-implanted helium (10 appm and 100 appm) using 5 MeV Fe++ ions. Their results showed swelling of CNS I ranged from 5.7% to 9%, while CNS II demonstrated lower swelling compared to CNSI and T91. The swelling of CNS II regardless of helium content was one to two magnitudes lower than CNS I. The irradiation induced formation of $(Fe,Cr)_2C$ was attributed to the superior swelling resistance of CNS II.

Although these findings are promising, further investigation is required to fully understand the behavior of the fabricated G-91 and G-92 steels under irradiation conditions, particularly regarding the influence of preexisting voids on void swelling and failure mechanisms. Long-term mechanical and thermal stability studies, in addition to investigations into key bulk radiation degradation effects (Zinkle and Was, 2013) are essential to thoroughly qualify these alloys for nuclear applications. Nonetheless, the fabrication of nearly fully dense samples produced with the optimal parameters and the achieved hardness levels serve as a strong foundation for continued research aimed at optimizing heat treatments to improve mechanical performance and validating long-term stability under representative nuclear operating conditions.

5 Conclusion

This study successfully demonstrated the laser powder DED printability of G-91 and for the first time G-92 steels, establishing the feasibility of achieving nearly fully dense components through optimized process parameters involving variations in laser power and scan speed, coupled with preliminary microstructural characterization and microhardness evaluation.

The findings are as follows:

- Optimal DED processing parameters for G-91 steel included a laser power range of 600–800 W and a scan speed of 500–800 mm/min, yielding average porosity levels between 0.03% and 1.89%.
- Optimal DED processing parameters for G-92 steel were identified as a laser power range of 500–800 W and a scan speed of 500–800 mm/min, resulting in average porosity levels ranging from 0.01% to 0.84%, except for the sample produced at 500 W and 500 mm/min, which exhibited a slight deviation.

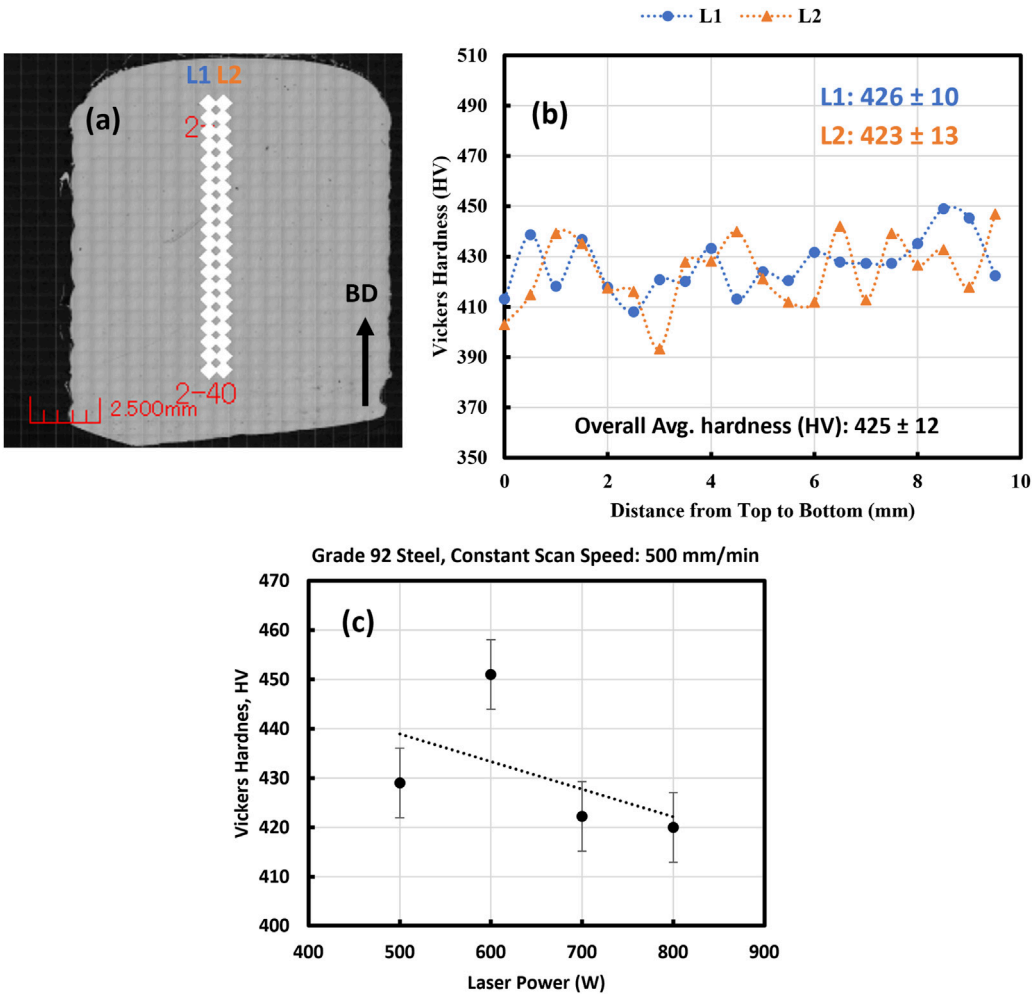

FIGURE 10
Representative Vickers hardness of Grade 92 steel: **(a)** optical micrograph with two arrays of indents (spacing between indents: 0.5 mm) L1, and L2 respectively, **(b)** Vickers hardness as a function of distance, and **(c)** Variation in Vickers hardness with laser power at a constant scan speed of 500 mm/min. The indentation patterns are schematic and not drawn to scale.

TABLE 4 Vickers hardness, estimated σ_y from Vickers Hardness, and reported σ_y from tensile testing of G-91, and G-92 Steels.

Alloys	Vickers hardness, (HV)	Estimated σ_y (MPa)	σ_y from tensile testing, (MPa)	Ref.
LPBF G-91, as-deposited	-	-	~773	Eftink et al. (2021b)
DED G-91, as-deposited	350 ± 21	~940	~900	Samuha et al. (2023a)
WAAM G-91, as-deposited	412 ± 23	~1150	-	Robin et al. (2024)
WAAM G-91, as-deposited	-	-	~1026	Sridharan and Field (2019b)
Wrought G-91	-	-	~600	Tong and Dai (2010)
T-91 steel tubes, As-received	237 ± 2.1	~557.41		Liu et al. (2015)
DED G-91, as-deposited	386 ± 14	~1063	-	This study
DED G-92, as-deposited	425 ± 12	~1195	-	This study
P-92, ASTM A335	-	-	Min. 440	Sklenička et al. (2015)
P-92 steel pipe, OD 350 × 39 mm^2	-	-	565	Sklenička et al. (2015)

- X-ray diffraction analysis confirmed the presence of BCC α-ferrite in both G-91 and G-92 steels, with potential peak overlap masking the martensite phase.
- Microstructural analysis revealed predominantly lath martensitic microstructures in both G-91 and G-92 steels. The presence of this characteristic microstructure is indicative of the rapid cooling rates associated with the DED process.
- The average Vickers hardness of G-91 steel was 386 ± 14 HV, while that of G-92 steel was 425 ± 12 HV, with minimal variation observed throughout the builds, suggesting consistent material properties and uniform consolidation across the fabricated components. The yield strength, estimated from the Vickers hardness measurements, was determined to be 1063 MPa for G-91 steel and 1195 MPa for G-92 steel.

Data availability statement

The original contributions presented in the study are included in the article/supplementary material, further inquiries can be directed to the corresponding authors.

Author contributions

AM: Conceptualization, Data curation, Formal Analysis, Investigation, Methodology, Validation, Visualization, Writing – original draft, Writing – review and editing. SM: Conceptualization, Data curation, Formal Analysis, Investigation, Methodology, Validation, Visualization, Writing – review and editing. PR: Investigation, Writing – review and editing. AR: Investigation, Writing – review and editing. CS: Investigation, Writing – review and editing. JS: Investigation, Writing – review and editing. QZ: Investigation, Writing – review and editing. XL: Investigation, Methodology, Resources, Supervision, Writing – review and editing. IV: Funding acquisition, Methodology, Project administration, Resources, Supervision, Validation, Visualization, Writing – review and editing.

Funding

The author(s) declare that financial support was received for the research and/or publication of this article. The research presented here was supported by the Advanced Materials and Manufacturing Technology (AMMT) program of the U.S. Department of Energy (DOE), Office of Nuclear Energy. Pacific Northwest National Laboratory (PNNL) is a multiprogram national laboratory operated for the DOE by Battelle Memorial Institute under Contract No. DE-AC05-76RL01830.

Acknowledgments

We express our sincere gratitude to Stuart Maloy for peer-reviewing this manuscript. The authors also acknowledge Alan L Schemer-Kohrn for his assistance with the acquisition of EBSD data. The authors would like to sincerely acknowledge the contribution of Nicholas Conway for his assistance in measuring the Archimedes density of selected G-91 and G-92 samples.

Conflict of interest

The authors declare that the research was conducted in the absence of any commercial or financial relationships that could be construed as a potential conflict of interest.

Generative AI statement

The author(s) declare that no Generative AI was used in the creation of this manuscript.

Any alternative text (alt text) provided alongside figures in this article has been generated by Frontiers with the support of artificial intelligence and reasonable efforts have been made to ensure accuracy, including review by the authors wherever possible. If you identify any issues, please contact us.

Publisher's note

References

Abe, F. (2008). Precipitate design for creep strengthening of 9% Cr tempered martensitic steel for ultra-supercritical power plants. *Sci. Technol. Adv. Mater.* 9, 013002. doi:10.1088/1468-6996/9/1/013002

Abe, F., and Nakazawa, S. (1992). The effect of tungsten on creep behavior of tempered martensitic 9Cr steels. *Metall. Trans. A* 23 (11), 3025–3034. doi:10.1007/bf02646120

Abràmoff, M. D., Magalhães, P. J., and Ram, S. J. (2004). Image processing with ImageJ. *Biophot. Int.* 11 (7), 36–42.

Ahn, D.-G. (2021). Directed energy deposition (DED) process: state of the art. *Int. J. Precis. Eng. Manufacturing-Green Technol.* 8 (2), 703–742. doi:10.1007/s40684-020-00302-7

Aprilia, A., Wu, N., and Zhou, W. (2022). Repair and restoration of engineering components by laser directed energy deposition. *Mater. Today Proc.* 70, 206–211. doi:10.1016/j.matpr.2022.09.022

Armas, A. F., Avalos, M., Alvarez-Armas, I., Peterson, C., and Schmitt, R. (1998). Dynamic strain ageing evidences during low cycle fatigue deformation in ferritic-martensitic stainless steels. *J. Nucl. Mater.* 258-263, 1204–1208. doi:10.1016/s0022-3115(98)00187-1

Bruce, D., Paradise, P., Saxena, A., Temes, S., Clark, R., Noe, C., et al. (2022). A critical assessment of the Archimedes density method for thin-wall specimens in laser powder bed fusion: measurement capability, process sensitivity and property correlation. *J. Manuf. Process.* 79, 185–192. doi:10.1016/j.jmapro.2022.04.059

Busby, J. T., Hash, M. C., and Was, G. S. (2005). The relationship between hardness and yield stress in irradiated austenitic and ferritic steels. *J. Nucl. Mater.* 336 (2-3), 267–278. doi:10.1016/j.jnucmat.2004.09.024

Cabet, C., Dalle, F., Gaganidze, E., Henry, J., and Tanigawa, H. (2019). Ferritic-martensitic steels for fission and fusion applications. *J. Nucl. Mater.* 523, 510–537. doi:10.1016/j.jnucmat.2019.05.058

Choudhary, B. K., and Isaac Samuel, E. (2011). Creep behaviour of modified 9Cr–1Mo ferritic steel. *J. Nucl. Mater.* 412 (1), 82–89. doi:10.1016/j.jnucmat.2011.02.024

Ciurana, J., Hernandez, L., and Delgado, J. (2013). Energy density analysis on single tracks formed by selective laser melting with CoCrMo powder material. *Int. J. Adv. Manuf. Technol.* 68 (5-8), 1103–1110. doi:10.1007/s00170-013-4902-4

Cui, L., Jiang, S., Xu, J., Peng, R. L., Mousavian, R. T., and Moverare, J. (2021). Revealing relationships between microstructure and hardening nature of additively manufactured 316L stainless steel. *Mater. and Des.* 198, 109385. doi:10.1016/j.matdes.2020.109385

Dass, A., and Moridi, A. (2019). State of the art in directed energy deposition: from additive manufacturing to materials design. *Coatings* 9 (7), 418. doi:10.3390/coatings9070418

De Terris, T., Castelnau, O., Hadjem-Hamouche, Z., Haddadi, H., Michel, V., and Peyre, P. (2021). Analysis of as-built microstructures and recrystallization phenomena on inconel 625 alloy obtained via laser powder bed fusion (L-PBF). *Metals* 11 (4), 619. doi:10.3390/met11040619

DebRoy, T., Wei, H., Zuback, J., Mukherjee, T., Elmer, J., Milewski, J., et al. (2018a). Additive manufacturing of metallic components–process, structure and properties. *Prog. Mater. Sci.* 92, 112–224. doi:10.1016/j.pmatsci.2017.10.001

DebRoy, T., Wei, H. L., Zuback, J. S., Mukherjee, T., Elmer, J. W., Milewski, J. O., et al. (2018b). Additive manufacturing of metallic components – process, structure and properties. *Prog. Mater. Sci.* 92, 112–224. doi:10.1016/j.pmatsci.2017.1.001

Demeneghi, G., Williams, B., Katsarelis, C., Tilson, W., and Gradl, P. (2025). Additively manufactured GRCop-42 copper-alloy combustion chamber failure analysis: the role of build interruptions. *Eng. Fail. Anal.* 177, 109710. doi:10.1016/j.engfailanal.2025.109710

Eftink, B. P., Vega, D. A., Atwani, O. E., Sprouster, D. J., Yoo, Y. S. J., Steckley, T. E., et al. (2021a). Tensile Properties and microstructure of additively manufactured Grade 91 steel for nuclear applications. *J. Nucl. Mater.* 544, 152723. doi:10.1016/j.jnucmat.2020.12723

Eftink, B. P., Vega, D. A., El Atwani, O., Sprouster, D. J., Yoo, Y. S. J., Steckley, T. E., et al. (2021b). Tensile properties and microstructure of additively manufactured Grade 91 steel for nuclear applications. *J. Nucl. Mater.* 544, 152723. doi:10.1016/j.jnucmat.2020.152723

El-Atwani, O., Eftink, B. P., Cady, C. M., Coughlin, D. R., Schneider, M. M., and Maloy, S. A. (2021). Enhanced mechanical properties of additive manufactured Grade 91 steel. *Scr. Mater.* 199, 113888. doi:10.1016/j.scriptamat.2021.113888

Eliasu, A., Czekanski, A., and Boakye-Yiadom, S. (2021). Effect of laser powder bed fusion parameters on the microstructural evolution and hardness of 316L stainless steel. *Int. J. Adv. Manuf. Technol.* 113 (9-10), 2651–2669. doi:10.1007/s00170-021-06818-9

Ennis, P. J., Zielinska-Lipiec, A., Wachter, O., and Czyrska-Filemonowicz, A. (1997). Microstructural stability and creep rupture strength of the martensitic steel P92 for advanced power plant. *Acta Mater.* 45 (12), 4901–4907. doi:10.1016/s1359-6454(97)00176-6

Fazio, C., Alamo, A., Almazouzi, A., De Grandis, S., Gomez-Briceno, D., Henry, J., et al. (2009). European cross-cutting research on structural materials for Generation IV and transmutation systems. *J. Nucl. Mater.* 392 (2), 316–323. doi:10.1016/j.jnucmat.2009.03.020

Feng, J., Zhang, P., Jia, Z., Yu, Z., Fang, C., Yan, H., et al. (2022). Laser additive manufacturing and post-heat treatment on microstructure and mechanical properties of 9Cr steel. *Int. J. Press. Vessels Pip.* 198, 104681. doi:10.1016/j.ijpvp.2022.104681

Fournier, B., Dalle, F., Sauzay, M., Longour, J., Salvi, M., Caës, C., et al. (2011). Comparison of various 9–12%Cr steels under fatigue and creep-fatigue loadings at high temperature. *Mater. Sci. Eng. A* 528 (22-23), 6934–6945. doi:10.1016/j.msea.2011.05.046

Frazier, W. E. (2014). Metal additive manufacturing: a review. *J. Mater. Eng. Perform.* 23 (6), 1917–1928. doi:10.1007/s11665-014-0958-z

Gao, H., Huang, Y., Nix, W. D., and Hutchinson, J. W. (1999). Mechanism-based strain gradient plasticity— I. Theory. *J. Mech. Phys. Solids* 47 (6), 1239–1263. doi:10.1016/s0022-5096(98)00103-3

Gelles, D. S. (1994). Microstructural development in reduced activation ferritic alloys irradiated to 200 dpa at 420 ˚C. *J. Nucl. Mater.* 212-215, 714–719. doi:10.1016/0022-3115(94)90150-3

Gradl, P., Tinker, D. C., Park, A., Mireles, O. R., Garcia, M., Wilkerson, R., et al. (2022). Robust metal additive manufacturing process selection and development for aerospace components. *J. Mater. Eng. Perform.* 31 (8), 6013–6044. doi:10.1007/s11665-022-06850-0

Gräning, T., and Sridharan, N. (2022). Benchmarking a 9Cr-2WVTa reduced activation ferritic martensitic steel fabricated via additive manufacturing. *Metals* 12 (2), 342. doi:10.3390/met12020342

Guguloth, K., and Roy, N. (2017). Creep deformation behavior of 9Cr1MoVNb (ASME Grade 91) steel. *Mater. Sci. Eng. A* 680, 388–404. doi:10.1016/j.msea.2016.10.112

Hald, J. (2008). Microstructure and long-term creep properties of 9–12% Cr steels. *Int. J. Press. Vessels Pip.* 85 (1-2), 30–37. doi:10.1016/j.ijpvp.2007.06.010

Hatakeyama, T., Sawada, K., Suzuki, M., and Watanabe, M. (2023). Microstructure development of modified 9Cr-1Mo steel during laser powder bed fusion and heat treatment. *Addit. Manuf.* 61, 103350. doi:10.1016/j.addma.2022.103350

Henry, J., and Maloy, S. A. (2017). "Irradiation-resistant ferritic and martensitic steels as core materials for Generation IV nuclear reactors," in *Structural materials for generation IV nuclear reactors*, 329–355.

Huang, Q., Wang, X., Sun, S., Liu, Y., Liao, H., Zheng, P., et al. (2022). Development of reduced activation ferritic/martensitic steels in China. *J. Nucl. Mater.* 568, 153887. doi:10.1016/j.jnucmat.2022.153887

Kaar, S., Steineder, K., Schneider, R., Krizan, D., and Sommitsch, C. (2021). New Ms-formula for exact microstructural prediction of modern 3rd generation AHSS chemistries. *Scr. Mater.* 200, 113923. doi:10.1016/j.scriptamat.2021.113923

Kimura, K., Kwak, K., Nambu, S., and Koseki, T. (2020). Nondestructive evaluation of macro segregation in creep strength enhanced 9Cr-1Mo-V-Nb steel. *Scr. Mater.* 188, 179–182. doi:10.1016/j.scriptamat.2020.07.039

Klueh, R. L., and Nelson, A. T. (2007). Ferritic/martensitic steels for next-generation reactors. *J. Nucl. Mater.* 371 (1-3), 37–52. doi:10.1016/j.jnucmat.207.05.005

Klueh, R. L., and Nelson, A. T. (2007). Ferritic/martensitic steels for next-generation reactors. *J. Nucl. Mater.* 371, 37–52. doi:10.1016/j.jnucmat.2007.05.005

Kohyama, A., Hishinuma, A., Gelles, D. S., Klueh, R. L., Dietz, W., and Ehrlich, K. (1996). Low-activation ferritic and martensitic steels for fusion application. *J. Nucl. Mater.* 233, 138–147. doi:10.1016/S0022-3115(96)00327-3

Konijnenberg, P. J., Zaefferer, S., and Raabe, D. (2015). Assessment of geometrically necessary dislocation levels derived by 3D EBSD. *Acta Mater.* 99, 402–414. doi:10.1016/j.actamat.2015.06.051

Kubin, L. P., and Mortensen, A. (2003). Geometrically necessary dislocations and strain-gradient plasticity: a few critical issues. *Scr. Mater.* 48 (2), 119–125. doi:10.1016/s1359-6462(02)00335-4

Kumar, N., Joseph, A. S., Mehrotra, P., and Yadav, S. D. (2022). An improved dislocation density reliant model to address the creep deformation of reduced activation ferritic martensitic steel. *Forces Mech.* 9, 100117. doi:10.1016/j.finmec.2022.100117

Laliberte, F., Li, M., Almer, J., and Liu, L. (2018). *In-situ* synchrotron X-ray study of microstructural evolution during creep deformation in Grade 91 steel. *Mater. Sci. Eng. A* 737, 115–123. doi:10.1016/j.msea.2018.09.033

Li, M., Natesan, K., Chen, W., and Momozaki, Y. (2023). "Sodium compatibility of recently-developed optimized Grade 92 steel for advanced fast reactors," in *International Conference on fast reactors and related fuel cycles: next generation nuclear systems for sustainable development* (IAEA), 10.

Little, E. A. (1993). Microstructural evolution in irradiated ferritic-martensitic steels: transitions to high dose behaviour. *J. Nucl. Mater.* 206 (2-3), 324–334. doi:10.1016/0022-3115(93)90131-h

Liu, J., Wilson, J., Strangwood, M., Davis, C. L., Peyton, A., and Parker, J. (2015). Electromagnetic evaluation of the microstructure of Grade 91 tubes/pipes. *Int. J. Press. Vessels Pip.* 132-133, 65–71. doi:10.1016/j.ijpvp.2015.05.009

Liu, R., Wang, Z., Sparks, T., Liou, F., and Newkirk, J. (2017). "Aerospace applications of laser additive manufacturing," in *Laser additive manufacturing*, 351–371.

Martin Hedges, N. C. (2006). Near-net-shape rapid manufacture and repair by LENS®. *Rapid Prototyp.* 12 (4), 1–13.

Moussa, C., Bernacki, M., Besnard, R., and Bozzolo, N. (2015). About quantitative EBSD analysis of deformation and recovery substructures in pure Tantalum. *IOP Conf. Ser. Mater. Sci. Eng.* 89, 012038. doi:10.1088/1757-899x/89/1/012038

Moussa, C., Bernacki, M., Besnard, R., and Bozzolo, N. (2017). Statistical analysis of dislocations and dislocation boundaries from EBSD data. *Ultramicroscopy* 179, 63–72. doi:10.1016/j.ultramic.2017.04.005

Murty, K. L., and Charit, I. (2008). Structural materials for Gen-IV nuclear reactors: challenges and opportunities. *J. Nucl. Mater.* 383 (1-2), 189–195. doi:10.1016/j.jnucmat.2008.08.044

Najmon, J. C., Raeisi, S., and Tovar, A. (2019). "Review of additive manufacturing technologies and applications in the aerospace industry," in *Additive manufacturing for the aerospace industry*, 7–31.

Niu, P., Li, R., Zhu, S., Wang, M., Chen, C., and Yuan, T. (2020). Hot cracking, crystal orientation and compressive strength of an equimolar CoCrFeMnNi high-entropy alloy printed by selective laser melting. *Opt. and Laser Technol.* 127, 106147. doi:10.1016/j.optlastec.2020.106147

Nye, J. F. (1953). Some geometrical relations in dislocated crystals. *Acta Metall.* 1 (2), 153–162. doi:10.1016/0001-6160(53)90054-6

Odette, G. R. (1988). On mechanisms controlling swelling in ferritic and martensitic alloys. *J. Nucl. Mater.* 155-157, 921–927. doi:10.1016/0022-3115(88)90442-4

Odette, G. R., Alinger, M. J., and Wirth, B. D. (2008). Recent developments in irradiation-resistant steels. *Annu. Rev. Mater. Res.* 38 (1), 471–503. doi:10.1146/annurev.matsci.38.060407.130315

Packan, N. H., Stoller, R. E., and Kumar, A. S. (1990). *Effects of radiation on materials: 14th international Symposium (volume I)*. West Conshohocken, PA : ASTM International.

Panait, C. G., Bendick, W., Fuchsmann, A., Gourgues-Lorenzon, A. F., and Besson, J. (2010). Study of the microstructure of the Grade 91 steel after more than 100,000 h of creep exposure at 600 ˚C. *Int. J. Press. Vessels Pip.* 87 (6), 326–335. doi:10.1016/j.ijpvp.2010.03.017

Pantleon, W. (2008). Resolving the geometrically necessary dislocation content by conventional electron backscattering diffraction. *Scr. Mater.* 58 (11), 994–997. doi:10.1016/j.scriptamat.2008.01.050

Robin, I. K., Sprouster, D. J., Sridharan, N., Snead, L. L., and Zinkle, S. J. (2024). Synchrotron based investigation of anisotropy and microstructure of wire arc additive manufactured Grade 91 steel. *J. Mater. Res. Technology-Jmr&T* 29, 5010–5021. doi:10.1016/j.jmrt.2024.02.230

Rui, S.-S., Han, Q.-N., Wang, X., Li, S., Ma, X., Su, Y., et al. (2021). Correlations between two EBSD-based metrics Kernel Average Misorientation and Image Quality on indicating dislocations of near-failure low alloy steels induced by tensile and cyclic deformations. *Mater. Today Commun.* 27, 102445. doi:10.1016/j.mtcomm.2021.102445

Saboori, A., Aversa, A., Marchese, G., Biamino, S., Lombardi, M., and Fino, P. (2019). Application of directed energy deposition-based additive manufacturing in repair. *Appl. Sci.* 9 (16), 3316. doi:10.3390/app9163316

Samuha, S., Bickel, J., Mukherjee, T., DebRoy, T., Lienert, T. J., Maloy, S. A., et al. (2023a). Mechanical performance and microstructure of the grade 91 stainless steel produced via Directed Energy deposition laser technique. *Mater. and Des.* 227, 111804. doi:10.1016/j.matdes.2023.111804

Samuha, S., Bickel, J., Mukherjee, T., DebRoy, T., Lienert, T. J., Maloy, S. A., et al. (2023b). Mechanical performance and microstructure of the grade 91 stainless steel produced via Directed Energy deposition laser technique. *Mater. and Des.* 227, 111804. doi:10.1016/j.matdes.2023.11104

Sau, M., Hintsala, E. D., Chen, Y., Stauffer, D. D., Maloy, S. A., Eftink, B. P., et al. (2022). High-throughput Nanoindentation mapping of additively manufactured T91 steel. *JOM* 74 (4), 1469–1476. doi:10.1007/s11837-022-05189-0

Sawada, K., Kushima, H., Tabuchi, M., and Kimura, K. (2011). Microstructural degradation of Gr.91 steel during creep under low stress. *Mater. Sci. Eng. A* 528 (16-17), 5511–5518. doi:10.1016/j.msea.2011.03.073

Scipioni Bertoli, U., Wolfer, A. J., Matthews, M. J., Delplanque, J.-P. R., and Schoenung, J. M. (2017). On the limitations of Volumetric energy density as a design parameter for selective laser melting. *Mater. and Des.* 113, 331–340. doi:10.1016/j.matdes.2016.10.037

Seran, J. L., Brachet, J. C., and Alamo, A. (2001). "Ferritic-martensitic steels for fast reactor cores," in *Encyclopedia of materials: Science and technology* (Elsevier Science Ltd.), 2863–2866.

Shang, C. G., Wang, M. L., Zhou, Z. C., Yagi, K., and Lu, Y. H. (2023). The microstructure evolution and its effect on creep behaviors in P92 steel under different stresses. *Mater. Charact.* 198, 112744. doi:10.1016/j.matchar.2023.112744

Shrestha, T., Basirat, M., Charit, I., Potirniche, G. P., and Rink, K. K. (2013). Creep rupture behavior of Grade 91 steel. *Mater. Sci. Eng. A* 565, 382–391. doi:10.1016/j.msea.2012.12.031

Shrestha, T., Alsagabi, S., Charit, I., Potirniche, G., and Glazoff, M. (2015). Effect of heat treatment on microstructure and hardness of grade 91 steel. *Metals* 5, 131–149. doi:10.3390/met5010131

Sklenicka, V. (2003). Long-term creep behavior of 9–12%Cr power plant steels. *Mater. Charact.* 51 (1), 35–48. doi:10.1016/j.matchar.2003.09.012

Sklenička, V., Kuchařová, K., Král, P., Kvapilová, M., Svobodová, M., and Čmakal, J. (2015). The effect of hot bending and thermal ageing on creep and microstructure evolution in thick-walled P92 steel pipe. *Mater. Sci. Eng. A* 644, 297–309. doi:10.1016/j.msea.2015.07.072

Sow, M. C., De Terris, T., Castelnau, O., Hamouche, Z., Coste, F., Fabbro, R., et al. (2020). Influence of beam diameter on laser powder bed fusion (L-PBF) process. *Addit. Manuf.* 36, 101532. doi:10.1016/j.addma.2020.101532

Sridharan, N., and Field, K. (2019a). A road map for the advanced manufacturing of ferritic-martensitic steels. *Fusion Sci. Technol.* 75, 264–274. doi:10.1080/15361055.2019.1577124

Sridharan, N., and Field, K. (2019b). A road map for the advanced manufacturing of ferritic-martensitic steels. *Fusion Sci. Technol.* 75 (4), 264–274. doi:10.1080/15361055.2019.157124

Sridharan, N., Gussev, M. N., and Field, K. (2019a). Performance of a ferritic/martensitic steel for nuclear reactor applications fabricated using additive manufacturing. *J. Nucl. Mater.* 521, 45–55. doi:10.1016/j.jnucmat.209.04.020

Sridharan, N., Gussev, M. N., and Field, K. G. (2019b). Performance of a ferritic/martensitic steel for nuclear reactor applications fabricated using additive manufacturing. *J. Nucl. Mater.* 521, 45–55. doi:10.1016/j.jnucmat.2019.04.020

Subramaniam Nellian, A., and Hock Lye Pang, J. (2022). Metal additive manufacturing repair study on rail steel with Stellite 6 powder. *Mater. Today Proc.* 70, 101–105. doi:10.1016/j.matpr.2022.08.552

Svetlizky, D., Zheng, B., Vyatskikh, A., Das, M., Bose, S., Bandyopadhyay, A., et al. (2022). Laser-based directed energy deposition (DED-LB) of advanced materials. *Mater. Sci. Eng. A* 840, 142967. doi:10.1016/j.msea.2022.142967

Taler, J., Weglowski, B., and Pilarczyk, M. (2017). Monitoring of thermal stresses in pressure components using inverse heat conduction methods. *Int. J. Numer. Methods Heat and Fluid Flow* 27 (3), 740–756. doi:10.1108/hff-03-2016-0091

Tan, L., Sokolov, M. A., Pawel, S. J., Sham, T. L., and Busby, J. T. (2022a). Varied enhancements in mechanical properties and sodium compatibility of Grade 92 by thermomechanical treatments. *Mater. Sci. Eng. A* 832, 142359. doi:10.1016/j.msea.2021.142359

Tan, L., Zhong, W., Yang, Y., Field, K. G., Sridharan, N., and Nelson, A. T. (2022b). Creep behavior of an additively manufactured 9Cr steel in the as-built condition. *J. Nucl. Mater.* 570, 153943. doi:10.1016/j.jnucmat.2022.153943

Toloczko, M. B., and Eiholzer, C. R. (1994). Irradiation creep and swelling of the US fusion heats of HT9 and 9Cr-1Mo to 208 dpa at ~400 ˚C. *J. Nucl. Mater.* 212-215, 604–607. doi:10.1016/0022-3115(94)90131-7

Toloczko, M. B., Garner, F. A., and Eiholzer, C. R. (1994). Irradiation creep and swelling of the US fusion heats of HT9 and 9Cr-1Mo to 208 dpa at ~ 400 ˚C. *J. Nucl. Mater.* 212-215, 604–607. doi:10.1016/0022-3115(94)0131-7

Tong, Z., and Dai, Y. (2010). The microstructure and tensile properties of ferritic/martensitic steels T91, Eurofer-97 and F82H irradiated up to 20dpa in STIP-III. *J. Nucl. Mater.* 398 (1-3), 43–48. doi:10.1016/j.jnucmat.2009.10.008

Tsuchiya, M., Izumiyama, M., Imai, Y., and Ucirc, N. (1965). Thermodynamic study on the transformation of austenite to martensite in the iron-high nitrogen or-carbon binary system. *J. Jpn. Inst. Metals* 29 (4), 427–433. doi:10.2320/jinstmet1952.29.4_427

Vaughan, M., Elverud, M., Ye, J., Seede, R., Gibbons, S., Flater, P., et al. (2023). Development of a process optimization framework for fabricating fully dense advanced high strength steels using laser directed energy deposition. *Addit. Manuf.* 67, 103489. doi:10.1016/j.addma.2023.103489

Villaret, F., Boulnat, X., Aubry, P., Zollinger, J., Fabregue, D., and de Carlan, Y. (2021a). Modelling of delta ferrite to austenite phase transformation kinetics in martensitic steels: application to rapid cooling in additive manufacturing. *Materiala* 18, 101157. doi:10.1016/j.mtla.2021.11157

Villaret, F., Boulnat, X., Aubry, P., Zollinger, J., Fabrègue, D., and de Carlan, Y. (2021b). Modelling of delta ferrite to austenite phase transformation kinetics in martensitic steels: application to rapid cooling in additive manufacturing. *Materialia* 18, 101157. doi:10.1016/j.mtla.2021.101157

Viswanathan, R., and Bakker, W. (2001). Materials for ultrasupercritical coal power plants-boiler materials: Part 1. *J. Mater. Eng. Perform.* 10(1), 81–95. doi:10.1361/105994901770345394

Wang, L., Li, M., and Almer, J. (2014). Investigation of deformation and microstructural evolution in Grade 91 ferritic–martensitic steel by *in situ* high-energy X-rays. *Acta Mater.* 62, 239–249. doi:10.1016/j.actamat.2013.10.003

Wang, X., Gong, J., Zhao, Y., Wang, Y., and Ge, Z. (2016a). Numerical Simulation to study the effect of arc travelling speed and welding sequences on residual stresses in welded sections of new ferritic P92 pipes. *High Temp. Mater. Process.* 35 (2), 121–128. doi:10.1515/htmp-2014-0170

Wang, X., Yan, Q., Was, G. S., and Wang, L. (2016b). Void swelling in ferritic-martensitic steels under high dose ion irradiation: exploring possible contributions to swelling resistance. *Scr. Mater.* 112, 9–14. doi:10.1016/j.scriptamat.2015.08.032

Wei, H., Mukherjee, T., Zhang, W., Zuback, J., Knapp, G., De, A., et al. (2021). Mechanistic models for additive manufacturing of metallic components. *Prog. Mater. Sci.* 116, 100703. doi:10.1016/j.pmatsci.2020.100703

Whitt, A., Seede, R., Ye, J., Elverud, M., Vaughan, M., Elwany, A., et al. (2023a). A process optimization framework for laser direct energy deposition: densification, microstructure, and mechanical properties of an Fe Cr alloy. *J. Manuf. Process.* 85 (Medium), 434–449. doi:10.1016/j.jmapro.202.11.028

Whitt, A., Seede, R., Ye, J., Elverud, M., Vaughan, M., Elwany, A., et al. (2023b). A process optimization framework for laser direct energy deposition: densification, microstructure, and mechanical properties of an FeCr alloy. *J. Manuf. Process.* 85, 434–449. doi:10.1016/j.jmapro.2022.11.028

Wilkinson, A. J., and Randman, D. (2010). Determination of elastic strain fields and geometrically necessary dislocation distributions near nanoindents using electron back scatter diffraction. *Philos. Mag.* 90 (9), 1159–1177. doi:10.1080/14786430903304145

Xia, Z., Xu, J., Shi, J., Shi, T., Sun, C., and Qiu, D. (2020). Microstructure evolution and mechanical properties of reduced activation steel manufactured through laser directed energy deposition. *Addit. Manuf.* 33, 101114. doi:10.1016/j.addma.2020.101114

Yadav, S. D., Kalácska, S., Dománková, M., Yubero, D. C., Resel, R., Groma, I., et al. (2016a). Evolution of the substructure of a novel 12% Cr steel under creep conditions. *Mater. Charact.* 115, 23–31. doi:10.1016/j.matchar.2016.03.015

Yadav, S. D., Sonderegger, B., Stracey, M., and Poletti, C. (2016b). Modelling the creep behaviour of tempered martensitic steel based on a hybrid approach. *Mater. Sci. Eng. A* 662, 330–341. doi:10.1016/j.msea.2016.03.071

Yadav, S. D., Scherer, T., Prasad Reddy, G. V., Laha, K., Sasikala, G., Albert, S. K., et al. (2018). Creep modelling of P91 steel employing a microstructural based hybrid concept. *Eng. Fract. Mech.* 200, 104–114. doi:10.1016/j.engfracmech.2018.07.027

Yang, D., Kan, X., Gao, P., Zhao, Y., Yin, Y., Zhao, Z., et al. (2021). Influence of porosity on mechanical and corrosion properties of SLM 316L stainless steel. *Appl. Phys. A* 128 (1), 51. doi:10.1007/s00339-021-05191-4

Yano, Y., Tanno, T., Sekio, Y., Oka, H., Ohtsuka, S., Uwaba, T., et al. (2016). Tensile properties and hardness of two types of 11Cr-ferritic/martensitic steel after aging up to 45,000 h. *Nucl. Mater. Energy* 9, 324–330. doi:10.1016/j.nme.2016.08.007

Zhang, H., Long, B., and Dai, Y. (2008). Metallography studies and hardness measurements on ferritic/martensitic steels irradiated in STIP. *J. Nucl. Mater.* 377 (1), 122–131. doi:10.1016/j.jnucmat.2008.02.037

Zhong, W., Sridharan, N., Isheim, D., Field, K. G., Yang, Y., Terrani, K., et al. (2021a). Microstructures and mechanical properties of a modified 9Cr ferritic-martensitic steel in the as-built condition after additive manufacturing. *J. Nucl. Mater.* 545, 152742. doi:10.1016/j.jnucmat.220.152742

Zhong, W., Sridharan, N., Isheim, D., Field, K. G., Yang, Y., Terrani, K., et al. (2021b). Microstructures and mechanical properties of a modified 9Cr ferritic-martensitic steel in the as-built condition after additive manufacturing. *J. Nucl. Mater.* 545, 152742. doi:10.1016/j.jnucmat.2020.152742

Zhong, W., Yang, Y., Field, K. G., Sridharan, N., Terrani, K., and Tan, L. (2021c). Microstructure and mechanical properties of high Mn-containing ferritic-martensitic alloys exposed to cyclical thermal treatment. *Mater. Sci. Eng. A* 813, 141143. doi:10.1016/j.msea.2021.141143

Zhou, X., Liu, C., Yu, L., Liu, Y., and Li, H. (2015). Phase transformation behavior and microstructural control of high-Cr martensitic/ferritic heat-resistant steels for power and nuclear plants: a review. *J. Mater. Sci. Technol.* 31, 235–242. doi:10.1016/j.jmst.2014.12.001

Zhou, L., Mehta, A., McWilliams, B., Cho, K., and Sohn, Y. (2019). Microstructure, precipitates and mechanical properties of powder bed fused inconel 718 before and after heat treatment. *J. Mater. Sci. and Technol.* 35 (6), 1153–1164. doi:10.1016/j.jmst.2018.12.006

Zinkle, S. J., and Was, G. S. (2013). Materials challenges in nuclear energy. *Acta Mater.* 61 (3), 735–758. doi:10.1016/j.actamat.2012.11.004